International Journal of Solids and Structures 202 (2020) 39–57

Contents lists available at ScienceDirect

International Journal of Solids and Structures

journal homepage: www.elsevier.com/locate/ijsolstr

Multiscale modeling accounting for inelastic mechanisms of fuzzy fiber composites with straight or wavy carbon nanotubes

George Chatzigeorgiou [a,*], Fodil Meraghni [a], Nicolas Charalambakis [b], Adil Benaarbia [a]

[a] Arts et Metiers Institute of Technology, CNRS, Université de Lorraine, LEM3-UMR 7239, F-57070 Metz, France
[b] Department of Civil Engineering, Aristotle University of Thessaloniki and Center for Research and Development of Advanced Materials CERDAM, AUTH-Texas A&M, GR 54124 Thessaloniki, Greece

ARTICLE INFO

Article history:
Received 6 April 2020
Received in revised form 14 May 2020
Accepted 15 May 2020
Available online 24 May 2020

Keywords:
Fuzzy fiber
Unidirectional composites
Composite cylinders assemblage
Effective properties
Inelastic fields

ABSTRACT

This paper proposes a micromechanical approach aimed at identifying the response of unidirectional fuzzy fiber composites undergoing inelastic fields. Fuzzy fibers are reinforcement fibers coated with radially aligned straight or wavy carbon nanotubes grown through chemical deposition process (PVD or CVD). Due to this nature, the composite with fuzzy fibers is described by three scales: i) the microscale consisting of carbon nanotubes and their surrounding matrix, ii) the mesoscale containing the fiber, the nanocomposite and the matrix, and iii) the macroscale related to the overall fuzzy fiber composite. The developed framework considers for the mesoscopic scale an analytical formulation, based on the composite cylinders assemblage (CCA) method, combining the principles of the Transformation Field Analysis (TFA) technique. A numerical example that includes comparisons with full field homogenization strategies confirms the accuracy of the framework to predict the overall response, as well as the average local fields of the constituents.

1. Introduction

The exceptional mechanical and physical properties of carbon nanotubes (CNTs) determined experimentally or estimated (Shen and Li, 2004; Xiao et al., 2005; Batra and Sears, 2007), encouraged the extensive research production for the development of CNT-reinforced composites. In this spirit, composites including fuzzy fibers, i.e. carbon, glass or ceramic fibers coated with CNTs (Fig. 1), have been recently the subject of a plethora of publications due to the increasing interest for applications in aerospace, energy, infrastructure and health monitoring, among other areas (Sager et al., 2009; Sebastian et al., 2014; Hart et al., 2017).

Several modeling efforts have been conducted the last decade to identify different types of behavior of such composites, namely elastic (Chatzigeorgiou et al., 2011; Kundalwal and Ray, 2011; Kundalwal and Ray, 2012; Chatzigeorgiou et al., 2012), thermoelastic (Kundalwal and Ray, 2014; Kundalwal and Meguid, 2015) and electromechanical (Seidel et al., 2014; Dhala and Ray, 2015; Ren et al., 2015). Since the fibers are coated with the nanotubes, the interlayer (usually called nanocomposite) can be seen as a composite consisting of carbon nanotubes in radial arrangement on the surface of fibers inside the matrix. Thus, the nanocomposite can be treated as a separate heterogeneous material with cylindrically orthotropic response. As a consequence, the fuzzy fiber can be studied as two concentric cylinders (fiber and nanocomposite) embedded into the matrix, with the coating layer being a heterogeneous medium. Thus, the total composite is a three scale medium, with micro-(CNTs embedded in matrix), meso-(fuzzy fiber embedded in matrix) and macro- (composite) scales (Fig. 2).

Experimental and theoretical studies on the interphase strength between the matrix and the reinforcement are an extensive research topic. The background for developing a theory of fiber composites with enhanced fibers was the development of elasticity solutions for heterogeneous cylindrical fibers and the determination of the elastic deformation of composite cylinders with cylindrically orthotropic layers. The fundamental solutions for fibers embedded in a matrix by Hashin and Rosen (1964), Christensen and Lo (1979), Avery and Herakovich (1986), Hashin (1990) allow for predicting effective elastic and thermoelastic properties. The composite cylinder assemblage (CCA) approach, introduced by Hashin and Rosen (1964), remains a powerful tool for the prediction of effective properties of fiber composites. The three phases model, consisting of a cylindrically orthotropic cylinder, a coating with several degrees of anisotropy and a matrix, has been studied

* Corresponding author.
E-mail addresses: georges.chatzigeorgiou@ensam.eu (G. Chatzigeorgiou), fodil.meraghni@ensam.eu (F. Meraghni), charalam@civil.auth.gr (N. Charalambakis), adil.benaarbia@ensam.eu (A. Benaarbia).

https://doi.org/10.1016/j.ijsolstr.2020.05.015
0020-7683/

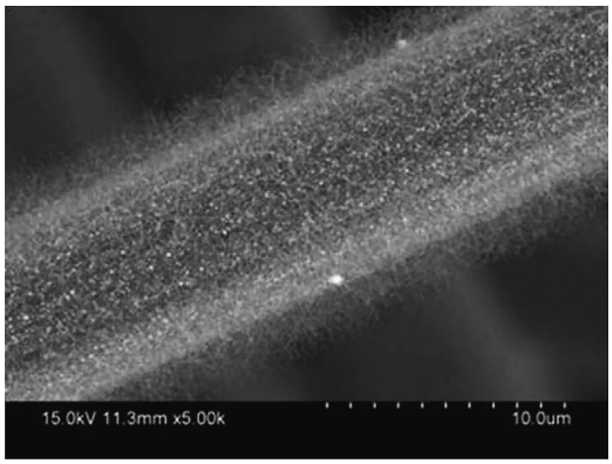

Fig. 1. A single fuzzy fiber with densely-packed CNTs on the surface. Reprinted by permission from Springer Nature: Multiscale Modeling of Multifunctional Fuzzy Fibers based on Multi-Walled Carbon Nanotubes, in "Modeling of Carbon Nanotubes, Graphene and their Composites", Tserpes, K. I., Silvestre, N. P. (Eds.), Vol. 188 of Springer Series in Materials Science, by Seidel G.D., Chatzigeorgiou G., Ren X., Lagoudas D.C., 2014.

and its effective thermoelastic behavior has been analyzed (Chen et al., 1990; Hashin, 1990).

The presence of a cylindrically orthotropic interphase layer in a fiber composite has been introduced by Honjo (2007). Explicit expressions for stress and displacements in a multilayered hollow cylinder with orthotropic elastic layers have been provided by Tsukrov and Drach (2010). The special case of a fiber composite in which each fiber is surrounded by cylindrically orthotropic layers has been investigated by Tsukrov et al. (2012) in order to analyze the influence of anisotropy and inhomogeneity of the layers on the fibers. In Chatzigeorgiou et al. (2011), a two step asymptotic expansion homogenization scheme in cylindrical (for the layer) and Cartesian coordinates has been presented. Chatzigeorgiou et al. (2012) proposed the approximate locally periodic homogenization for fiber composites with cylindrical geometry. In Chatzigeorgiou et al. (2012), the same problem has been investigated via the CCA method. In the latter article, the reinforced interphase is assumed to behave as a transversely isotropic medium with the axis of symmetry parallel to the axis of CNTs. Kundalwal and Ray (2011) have analyzed the fuzzy fiber composite response using Mori–Tanaka, by substituting the interphase layer with an equivalent transversely isotropic medium with the axis of symmetry parallel to the axis of the fiber. The same authors have proposed an alternative approach based on the method of cells (Kundalwal and Ray, 2012) to investigate the influence of the CNTs waviness on the overall response of the fuzzy fiber composites (Kundalwal and Ray, 2014).

The present paper proposes a micromechanical approach for unidirectional fuzzy fiber composites accounting for the presence of inelastic fields. The fuzzy fibers are considered to be fibers coated with CNTs, which are either straight or wavy microfibers. The developed scheme is based on the CCA method, adopted for the cylindrically orthotropic nature of the nanocomposite layer that surrounds the actual fiber. Accounting for nonlinear mechanisms in analytical micromechanical approaches is a task studied by many authors in the literature. A popular approach addressing inelastic fields in composites is the well known transformation field analysis (TFA) by Dvorak (1992), Dvorak and Benveniste (1992), Michel and Suquet (2003). According to this approach, the stress or the strain is split into elastic and inelastic parts. In Chatzigeorgiou and Meraghni (2019), a mean field multiscale approach for composites reinforced by coated fibers exhibiting elastic and inelastic strain has been presented. It follows the TFA framework and performs two methodologies; one is based on classical Eshelby-type methods like Mori–Tanaka, while the second is based on the Composite Cylinders/Spheres Assemblage homogenization strategy. The TFA approach is extensively deployed in the present work for accounting the inelastic fields applied to the fuzzy fiber composite.

The organization of the paper is as follows: In Section 2, the problem under consideration is described, including a general description of the fuzzy fiber composites, the assumptions on the material symmetries of the phases and the equations of the problem. Section 3 presents the composite cylinders assemblage methodology for the mesoscale problem. In Section 4, a numerical example of a fuzzy fiber composite with wavy carbon nanotubes is presented. The conclusions section closes the main part of the manuscript. The transformation rules between Cartesian and cylindrical coordinate systems and computational details regarding the elastic and inelastic concentration tensors are summarized in two Appendices.

2. Problem definition

The scope of this section is to describe the problem under consideration. Before identifying the various scales, some preliminary notes are required concerning the coordinate systems that are utilized.

2.1. Preliminaries

Due to the geometrical characteristics of the fuzzy fiber composite, the theoretical development appears in two different orthogonal coordinate systems, the Cartesian and the cylindrical. In cylindrical coordinates, the axes (x_1, x_2, x_3) are transformed to (r, θ, z), according to the relations

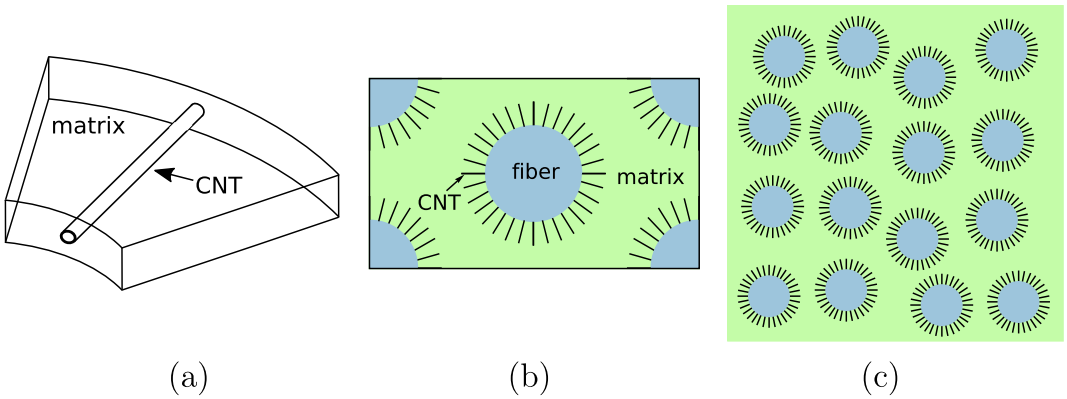

Fig. 2. Microscopic (a), mesoscopic (b) and macroscopic (c) scales of a fuzzy fiber composite material.

$x_1 = r\cos\theta, \quad x_2 = r\sin\theta, \quad x_3 = z.$

For second order tensors, the adopted Voigt notation considers the following representation: In Cartesian coordinates, $1, 2$ and 3 denote the normal components at the directions $1, 2$ and 3 respectively, while the shear components $4, 5$ and 6 denote the shear angles in $12, 13$ and 23 respectively. In cylindrical coordinates, $1, 2$ and 3 denote the normal components at the directions r, θ and z respectively, while the shear components $4, 5$ and 6 denote the shear angles in $r\theta, rz$ and θz respectively. Thus, the various fields are expressed in vector form in the Cartesian system as

$$\begin{aligned}
\boldsymbol{u} &= [\,u_1 \quad u_2 \quad u_3\,]^T,\\
\boldsymbol{\varepsilon} &= [\,\varepsilon_{11} \quad \varepsilon_{22} \quad \varepsilon_{33} \quad 2\varepsilon_{12} \quad 2\varepsilon_{13} \quad 2\varepsilon_{23}\,]^T,\\
\boldsymbol{\sigma} &= [\,\sigma_{11} \quad \sigma_{22} \quad \sigma_{33} \quad \sigma_{12} \quad \sigma_{13} \quad \sigma_{23}\,]^T,
\end{aligned}$$

and in the cylindrical system as

$$\begin{aligned}
\boldsymbol{u}^{\text{cyl}} &= [\,u_r \quad u_\theta \quad u_z\,]^T,\\
\boldsymbol{\varepsilon}^{\text{cyl}} &= [\,\varepsilon_{rr} \quad \varepsilon_{\theta\theta} \quad \varepsilon_{zz} \quad 2\varepsilon_{r\theta} \quad 2\varepsilon_{rz} \quad 2\varepsilon_{\theta z}\,]^T,\\
\boldsymbol{\sigma}^{\text{cyl}} &= [\,\sigma_{rr} \quad \sigma_{\theta\theta} \quad \sigma_{zz} \quad \sigma_{r\theta} \quad \sigma_{rz} \quad \sigma_{\theta z}\,]^T.
\end{aligned}$$

The transformation of the fields between the two coordinate systems require proper rotation tensors, which are presented in Appendix A.

2.2. General description of the fuzzy fiber composite

Figs. 3$_a$ and 3$_c$ illustrate typical unidirectional fuzzy fiber composites, in which the main fibers (made by carbon, glass or other material) are coated with radially aligned straight (Fig. 3$_b$) or wavy (Fig. 3$_d$) carbon nanotubes (CNTs). The CNTs are represented as hollow microfibers. The fibers and the nanocomposite interphase (CNT + matrix) are arranged in such a way that they form a unidirectional lamina layer and are dispersed randomly inside the matrix.

The fibers (phase 1) and the matrix (phase 0) are assumed to be at most transversely isotropic with axis of symmetry parallel to the axis of the fibers. Thus, their elasticity tensors are expressed in the form

$$\boldsymbol{L}_i = \boldsymbol{L}_i^{\text{cyl}} = \begin{bmatrix}
K_i^{\text{tr}} + \mu_i^{\text{tr}} & K_i^{\text{tr}} - \mu_i^{\text{tr}} & l_i & 0 & 0 & 0\\
K_i^{\text{tr}} - \mu_i^{\text{tr}} & K_i^{\text{tr}} + \mu_i^{\text{tr}} & l_i & 0 & 0 & 0\\
l_i & l_i & n_i & 0 & 0 & 0\\
0 & 0 & 0 & \mu_i^{\text{tr}} & 0 & 0\\
0 & 0 & 0 & 0 & \mu_i^{\text{ax}} & 0\\
0 & 0 & 0 & 0 & 0 & \mu_i^{\text{ax}}
\end{bmatrix}, \quad i = 0, 1.$$

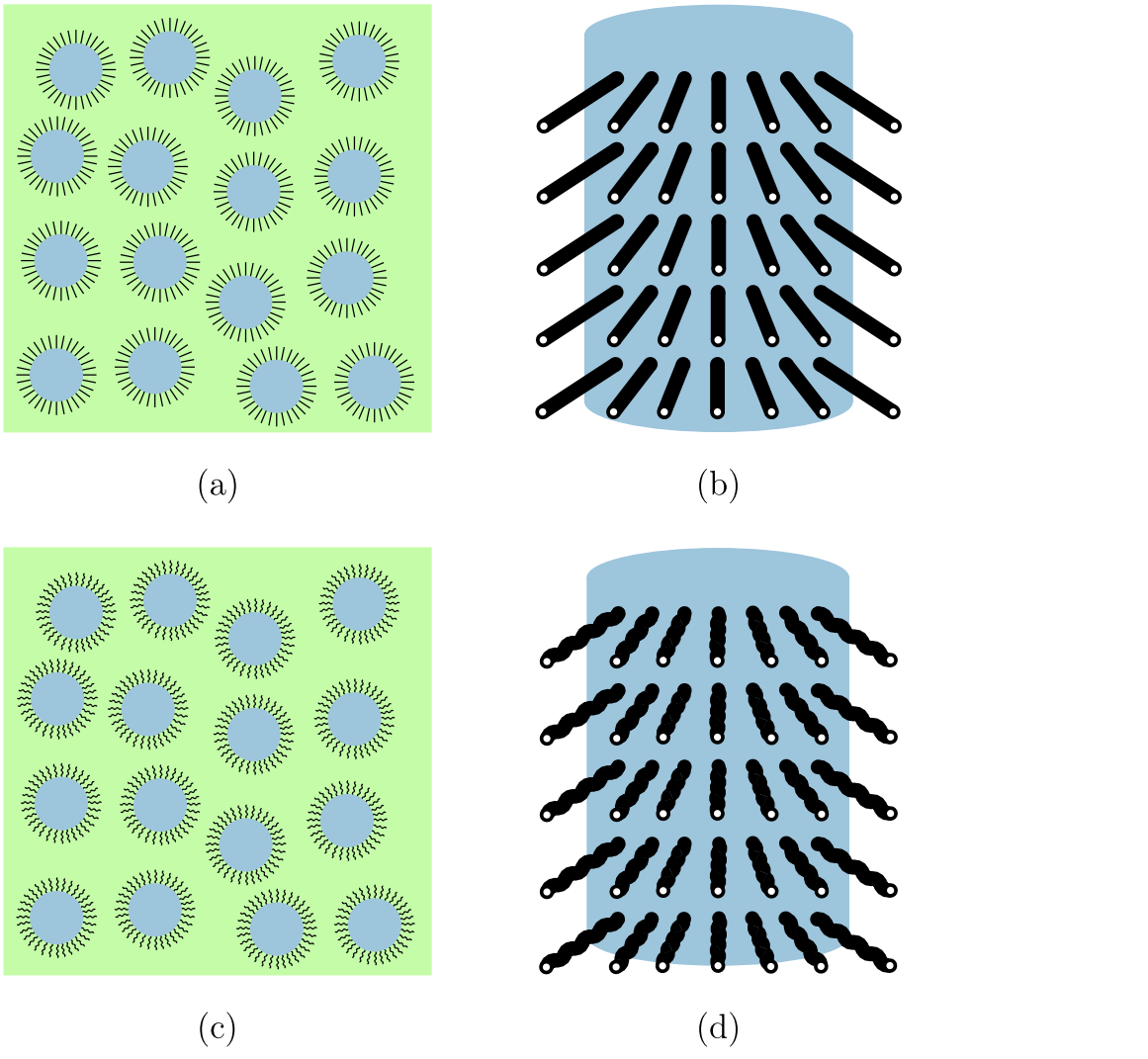

Fig. 3. (a) Unidirectional fuzzy fiber composite with straight carbon nanotubes. (b) Schematic of fuzzy fiber with straight carbon nanotubes. (c) Unidirectional fuzzy fiber composite with wavy carbon nanotubes. (d) Schematic of fuzzy fiber with wavy carbon nanotubes.

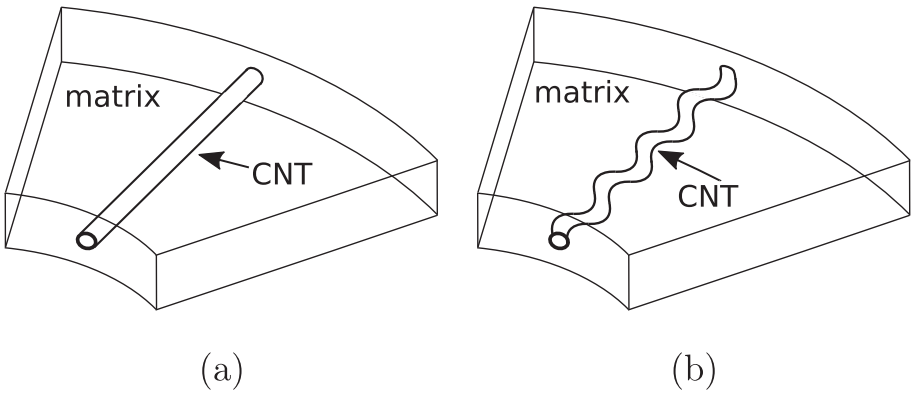

Fig. 4. Microscale of the fuzzy fiber composite: (a) straight or (b) wavy carbon nanotubes in matrix.

The material properties for these phases are the transverse bulk modulus[1], K_i^{tr}, the transverse shear modulus, μ_i^{tr}, the axial shear modulus, μ_i^{ax}, and the coefficients l_i and n_i. These are considered known. It is noted that due to their construction (at most transversely isotropic in the fiber direction), the above elasticity tensors remain unchanged during the transition from cylindrical to Cartesian coordinates.

The fuzzy fiber composite can be considered as a three phase medium (Fig. 2) consisting of the homogeneous fiber, the matrix and the heterogeneous interphase (nanocomposite). The latter contains the CNTs and matrix material. The multiscale approach that is utilized for such medium consists of two steps. The first homogenization step is performed on the nanocomposite and the new medium is treated as a homogenized coating layer attached to the main fibers. In the second step, the fibers, the coating and the matrix constitute the mesoscale. Homogenization at the mesoscale leads at obtaining the overall properties of the fuzzy fiber composite.

2.3. Microscale: CNTs embedded in matrix (nanocomposite)

Fig. 4 demonstrates a sketch of the microstructure of the nanocomposite. Its geometrical characteristics differ for straight (Fig. 4_a) or wavy (Fig. 4_b) CNTs. This subsection briefly discusses the method for obtaining the effective properties of the nanotube reinforced interphase.

The diameter of the CNTs is at the order of nanotubes. Thus, the validity of continuum mechanics concepts at such small scales is questionable. However, classical homogenization strategies for carbon nanotube reinforced composites are adopted frequently in the literature with quite satisfactory results (Seidel and Lagoudas, 2006).

The cylindrical structure of the nanocomposites' RVE poses certain challenges in terms of homogenization. To properly study such reinforced interphase via periodic homogenization, one has to consider that this composite presents cylindrical periodicity, in which the structure cannot be obtained by repetition of the same unit cell, as in Cartesian periodic composites. In addition, the volume fraction of the CNTs inside the matrix is reduced with the increase of the radial direction.

The most accurate technique for such microstructure is the asymptotic expansion homogenization, interpreted in cylindrical coordinates by Chatzigeorgiou et al. (2011) and for more complex microstructures the generalized periodicity homogenization (Tsalis et al., 2012; Guinovart-Sanjuán et al., 2016). The importance of cylindrical meso- and micro-coordinates is outlined in the above papers, since they allow to consider a 2-D cell problem and represent in a consistent way the homogenization process for shell structures by exploiting the locally periodic homogenization techniques. The periodic microstructure depends on the radial distance, therefore the approximate locally periodic homogenization technique described in Tsalis et al. (2012) leads to a continuously graded effective material. This homogenization technique is applied to several unit cells, whose effective properties are computed numerically.

Another important aspect in the behavior of a nanocomposite is the possible agglomeration of carbon nanotubes. This phenomenon has been studied extensively in the literature of nanocomposites (Ma et al., 2008; Al-Saleh and Sundararaj, 2011). High volume fraction of CNTs that are not well dispersed can even cause decrease in the composite's overall behavior (Bal and Samal, 2007). With regard to fuzzy fiber composites, high CNT content (over 40%) at the interphase between the fibers and the matrix has been reported in some studies (Chatzigeorgiou et al., 2012; Ren et al., 2015; Zhou et al., 2016). To the best of the authors knowledge, the effects of CNTs agglomeration on the interphase regions of fuzzy fiber composites have not been investigated. In this manuscript, such aspects are not considered. However, one can account for agglomeration of CNTs through various micromechanics techniques (Seidel and Lagoudas, 2006; Feng et al., 2007).

The results of the computational homogenization indicate that the effective nanocomposite is cylindrically orthotropic with its coefficients spatially dependent on the mesoscale radial distance. In a rough but rather successful approximation, it is assumed that the nanocomposite behaves as a typical unidirectional fiber composite (see Seidel et al., 2014). This last assumption is also adopted in the present work. When the CNTs are wavy, the unidirectional microfiber composite properties can be identified through computational (Kundalwal and Ray, 2014; Tsalis et al., 2017) or analytical (Yanase et al., 2013; Zhu et al., 2020) strategies.

In general, the microfibers are distributed on the fiber surface in a random way. For computational purposes, one can consider either tetragonal or hexagonal array packing of microfibers. The homogenized nanocomposite (phase 2) presents cylindrical orthotropy and its elasticity tensor is expressed as

$$\boldsymbol{L}_2^{\mathrm{cyl}} = \begin{bmatrix} L_2^{rr} & L_2^{r\theta} & L_2^{rz} & 0 & 0 & 0 \\ L_2^{r\theta} & L_2^{\theta\theta} & L_2^{\theta z} & 0 & 0 & 0 \\ L_2^{rz} & L_2^{\theta z} & L_2^{zz} & 0 & 0 & 0 \\ 0 & 0 & 0 & \mu_2^{r\theta} & 0 & 0 \\ 0 & 0 & 0 & 0 & \mu_2^{rz} & 0 \\ 0 & 0 & 0 & 0 & 0 & \mu_2^{\theta z} \end{bmatrix}.$$

The 9 material coefficients of this medium are $L_2^{rr}, L_2^{\theta\theta}, L_2^{zz}, L_2^{r\theta}, L_2^{rz}, L_2^{\theta z}$, $\mu_2^{r\theta}, \mu_2^{rz}$ and $\mu_2^{\theta z}$.

[1] It should not be confused with the traditional bulk modulus of isotropic materials.

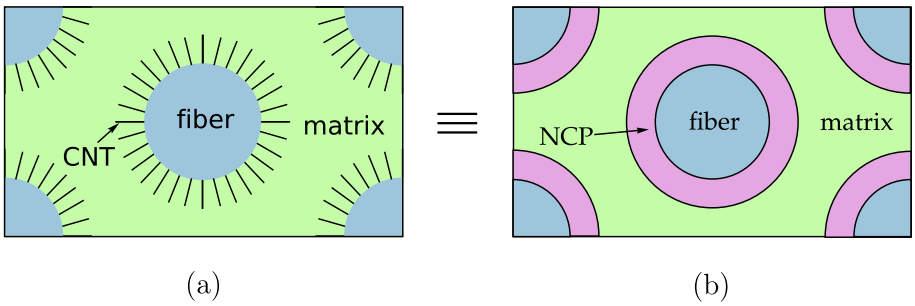

Fig. 5. Mesoscale of the fuzzy fiber composite: (a) Hexagonal arrangement of fuzzy fibers. (b) Equivalent RVE where the CNTs and the surrounding matrix are substituted by a an interphase layer, the nanocomposite (NCP).

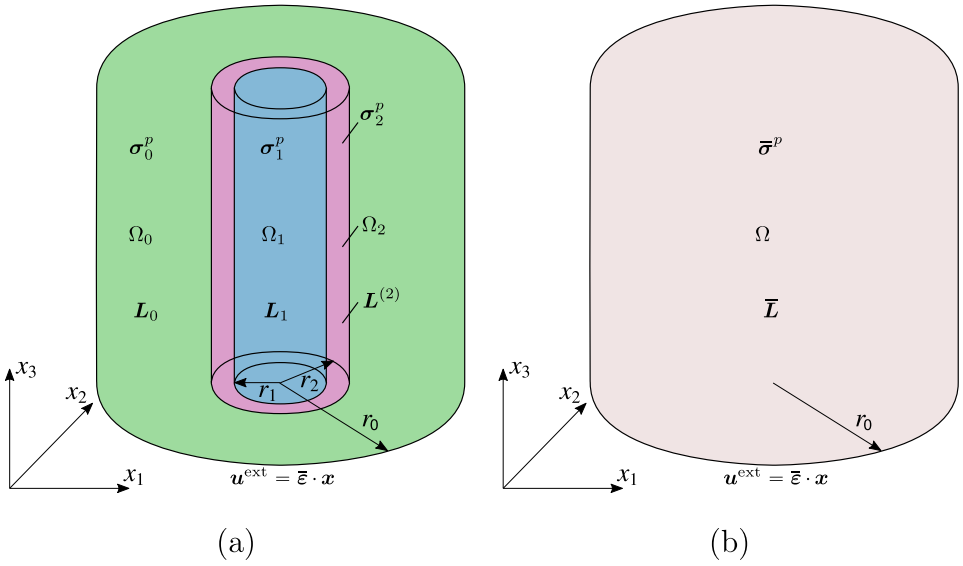

Fig. 6. (a) Coated cylindrical fiber, embedded in a matrix material. The fiber, the coating and the matrix have homothetic topology. The fiber and the matrix have constant elasticity moduli and uniform inelastic stresses, while the coating has spatially varying elastic modulus and uniform inelastic stress. Moreover, the system is subjected to linear macroscopic displacement. (b) Equivalent medium with equivalent uniform inelastic stress under the same boundary conditions.

2.4. Mesoscale: fuzzy fiber embedded in matrix

The random arrangement of the unidirectional fuzzy fibers in the matrix (Fig. 3) can be approximated in the mesoscale RVE by a distribution in a hexagonal array, as in Fig. 5$_a$ (see the discussion in Hashin and Rosen, 1964). After the first homogenization step at the microscale, the CNTs and their surrounding matrix are substituted by the equivalent nanocomposite (Fig. 5$_b$). The latter mesoscale RVE can be treated numerically through the periodic homogenization, but the computational cost is quite important due to the spatially dependent behavior, in Cartesian coordinates, of the nanocomposite. When dealing with the composite cylinders assemblage (CCA) approach, an equivalent RVE of concentric cylinders is introduced, as in Fig. 6$_a$.

In Tsukrov et al. (2012), Chatzigeorgiou et al. (2012), the CCA method has been used for evaluating the effective coefficients. By considering the mechanical response of the model to elementary load cases (axial tension, transverse hydrostatic tension, axial and transverse shear, thermal expansion) the effective thermomechanical behavior has been determined. Additionally, to evaluate the effective transverse shear modulus, the generalized self consistent method has been applied, in which a composite cylinder is surrounded by a transversely isotropic infinite matrix, whose shear modulus is equal to the unknown modulus, subjected to remote shear strain.

In this contribution, the main novelty compared to the previous works on the fuzzy fiber composites modeling of Chatzigeorgiou et al. (2011), Chatzigeorgiou et al. (2012), Chatzigeorgiou et al. (2012), Kundalwal and Ray (2011), Kundalwal and Ray (2012), Kundalwal and Ray (2014) is the integration of the TFA framework into the homogenization scheme. The proposed methodology accounts for nonlinear mechanisms through the presence of inelastic stress fields. To the best of the authors knowledge, the transformation field analysis has not been used in the literature before for the study of fuzzy fiber composites. The current approach permits to incorporate nonlinear mechanisms into the material constituents and to obtain appropriate concentration tensors, which provide the link between mesoscopic and macroscopic fields.

Consider a coated cylindrical inhomogeneity, embedded in a matrix material. The inhomogeneity is characterized by constant elasticity modulus $\boldsymbol{L}_1$, occupies the space Ω_1 with volume V_1, bounded by the surface $\partial\Omega_1$ and subjected to the uniform inelastic stress $\boldsymbol{\sigma}_1^p$. The coating layer is characterized by spatially varying elasticity modulus $\boldsymbol{L}^{(2)}(\boldsymbol{x})$, occupies the space Ω_2 with volume V_2, bounded by the surfaces $\partial\Omega_1$ and $\partial\Omega_2$ and subjected to the uniform inelastic stress $\boldsymbol{\sigma}_2^p$. It should be noted that, since the coating is cylindrically orthotropic, $\boldsymbol{L}^{(2)}$ is spatially dependent in Cartesian coordinates. The matrix is characterized by constant elasticity modulus $\boldsymbol{L}_0$, occupies the space Ω_0 with volume V_0, bounded by

the surface $\partial\Omega_0$ and subjected to the uniform inelastic stress $\boldsymbol{\sigma}_0^p$. At the boundary of the coating, a linear displacement field $\boldsymbol{u}^{\text{ext}} = \bar{\boldsymbol{\varepsilon}} \cdot \boldsymbol{x}$ is applied (Fig. 6$_a$), where $\bar{\boldsymbol{\varepsilon}}$ denotes the macroscopic strain tensor. As shown in Figs. 6$_a$ and 6$_b$, the space $\Omega = \Omega_1 \cup \Omega_2 \cup \Omega_0$ denotes the total RVE, whose volume is $V = V_1 + V_2 + V_0$.

For this RVE, the equilibrium equation reads

$$\text{div}\boldsymbol{\sigma} = \boldsymbol{0}, \quad \text{in } \Omega, \tag{1}$$

with

$$\boldsymbol{\sigma}(\boldsymbol{x}) = \begin{cases} \boldsymbol{L}_1 : \boldsymbol{\varepsilon}(\boldsymbol{x}) + \boldsymbol{\sigma}_1^p, & \boldsymbol{x} \in \Omega_1, \\ \boldsymbol{L}^{(2)}(\boldsymbol{x}) : \boldsymbol{\varepsilon}(\boldsymbol{x}) + \boldsymbol{\sigma}_2^p, & \boldsymbol{x} \in \Omega_2, \\ \boldsymbol{L}_0 : \boldsymbol{\varepsilon}(\boldsymbol{x}) + \boldsymbol{\sigma}_0^p, & \boldsymbol{x} \in \Omega_0. \end{cases} \tag{2}$$

In the proposed analytical micromechanics scheme, an equivalent medium with unknown elasticity tensor $\bar{\boldsymbol{L}}$ is considered to occupy the total space Ω, and is subjected: i) to the same displacement field at the boundary, and ii) to the uniform unknown inelastic stress $\bar{\boldsymbol{\sigma}}^p$ (Fig. 6$_b$). The main goal is to identify the macroscopic constitutive law for this medium,

$$\bar{\boldsymbol{\sigma}} = \bar{\boldsymbol{L}} : \bar{\boldsymbol{\varepsilon}} + \bar{\boldsymbol{\sigma}}^p. \tag{3}$$

The macroscopic stress and strain fields obey the standard relations with their microscopic counterparts

$$\bar{\boldsymbol{\varepsilon}} = \sum_{i=0}^{2} c_i \boldsymbol{\varepsilon}_i, \quad \bar{\boldsymbol{\sigma}} = \sum_{i=0}^{2} c_i \boldsymbol{\sigma}_i, \tag{4}$$

where the $\boldsymbol{\varepsilon}_i$ and $\boldsymbol{\sigma}_i$ denote average quantities per phase,

$$\boldsymbol{\varepsilon}_i = \frac{1}{V_i} \int_{\Omega_i} \boldsymbol{\varepsilon}(\boldsymbol{x})\, d\boldsymbol{x}, \quad \boldsymbol{\sigma}_i = \frac{1}{V_i} \int_{\Omega_i} \boldsymbol{\sigma}(\boldsymbol{x})\, d\boldsymbol{x}, \tag{5}$$

for i = 0,1,2 with c_i denoting the volume fractions of the material constituents. The applied macroscopic strain, $\bar{\boldsymbol{\varepsilon}}$, and the inelastic stresses, $\boldsymbol{\sigma}_1^p, \boldsymbol{\sigma}_2^p, \boldsymbol{\sigma}_0^p$, are known. The tasks of the analytical homogenization strategy are:

- To identify strain-type elastic, $\boldsymbol{A}_i$, and inelastic, $\boldsymbol{A}_{j,i}^p$, concentration tensors that satisfy the relations

$$\boldsymbol{\varepsilon}_i = \boldsymbol{A}_i : \bar{\boldsymbol{\varepsilon}} + \sum_{j=0}^{2} \boldsymbol{A}_{j,i}^p : \boldsymbol{\sigma}_j^p, \quad i = 0, 1, 2. \tag{6}$$

- To identify stress-type elastic, $\boldsymbol{D}_i$, and inelastic, $\boldsymbol{D}_{j,i}^p$, concentration tensors that satisfy the relations

$$\boldsymbol{\sigma}_i = \boldsymbol{D}_i : \bar{\boldsymbol{\varepsilon}} + \sum_{j=0}^{2} \boldsymbol{D}_{j,i}^p : \boldsymbol{\sigma}_j^p, \quad i = 0, 1, 2. \tag{7}$$

Combining (3), (4)$_2$ and (7) yields

$$\bar{\boldsymbol{L}} = \sum_{i=0}^{2} c_i \boldsymbol{D}_i, \quad \bar{\boldsymbol{\sigma}}^p = \sum_{j=0}^{2} \boldsymbol{B}_j^p : \boldsymbol{\sigma}_j^p, \quad \boldsymbol{B}_j^p = \sum_{i=0}^{2} c_i \boldsymbol{D}_{j,i}^p. \tag{8}$$

$\boldsymbol{B}_j^p$ denote the inelastic stress concentration tensors. In the development of the expressions (2)–(8) the crucial hypothesis is the uniformity of the inelastic fields inside the phases. Generally, the inelastic stresses in the matrix and in the nanocomposite are expected to be strongly nonuniform. However, considering uniform inelastic stresses, $\boldsymbol{\sigma}_i^p$, in all material phases is an unavoidable assumption for the development of analytical micromechanics strategies. The inelastic stresses are considered to represent the average inelastic stresses in a phase[2]. The constitutive law (2) combined with the expressions (6) "mimic" the classical TFA approach adopted in mean-field homogenization frameworks, like Mori–Tanaka. From a computational point of view, this hypothesis permits to easily account for nonlinear mechanisms like plasticity, viscoplasticity etc. Indeed, an iterative multiscale computational scheme for nonlinear materials uses the macroscopic strain field and expressions of the form (6) to identify the average strains per phase. The latter are utilized for predicting the inelastic stresses per phase.

The nonuniform spatial distribution of the inelastic fields inside the matrix phase is a known issue in the micromechanics community and usually leads to stiff macroscopic responses if classical approaches are followed. Certain methodologies have been proposed in the literature to overcome these stiff predictions (see for instance Chaboche et al., 2005; Lahellec and Suquet, 2007; Brassart et al., 2012; Barral et al., 2020; Wu et al., 2017).

Inside the nanocomposite, the non-uniformity of inelastic fields is expected to be strong due to its cylindrically orthotropic nature. In the present manuscript, the studied numerical examples examine the accuracy of the framework under known inelastic fields. In a forthcoming publication, the developed framework is going to be applied for composites with nonlinear fiber and coating phases, in which the inelastic fields are computed through appropriate incremental iterative schemes.

As a side note, thermal stresses are a special case of known inelastic fields which are incompatible with (2). To address this incompatibility, a special boundary value problem is studied in Section 3.

3. Mesoscale RVE: effective properties and concentration tensors

3.1. Expressing the mesoscale problem in cylindrical coordinates

Inside the RVE of Fig. 6$_a$, the various mechanical fields generated at every phase q ($q = 1, 2$) depend on the spatial position, i.e.[3]

$$\boldsymbol{u}^{(q)}(\boldsymbol{x}), \quad \boldsymbol{\varepsilon}^{(q)}(\boldsymbol{x}), \quad \boldsymbol{\sigma}^{(q)}(\boldsymbol{x}), \quad \boldsymbol{\sigma}^{p(q)}(\boldsymbol{x}), \quad \forall \boldsymbol{x} \in \Omega_q.$$

Due to the geometry of the inhomogeneities, the problem can be transformed in cylindrical coordinates, using a system of concentric cylinders for the fiber and the nanocomposite. In the cylindrical coordinate system, the strain tensor components at each phase are given by the expressions

$$\begin{aligned} \varepsilon_{rr}^{(q)} &= \frac{\partial u_r^{(q)}}{\partial r}, \quad \varepsilon_{\theta\theta}^{(q)} = \frac{1}{r}\frac{\partial u_\theta^{(q)}}{\partial \theta} + \frac{u_r^{(q)}}{r}, \quad \varepsilon_{zz}^{(q)} = \frac{\partial u_z^{(q)}}{\partial z}, \\ 2\varepsilon_{r\theta}^{(q)} &= \frac{\partial u_\theta^{(q)}}{\partial r} + \frac{1}{r}\frac{\partial u_r^{(q)}}{\partial \theta} - \frac{u_\theta^{(q)}}{r}, \quad 2\varepsilon_{rz}^{(q)} = \frac{\partial u_z^{(q)}}{\partial r} + \frac{\partial u_r^{(q)}}{\partial z}, \\ 2\varepsilon_{\theta z}^{(q)} &= \frac{1}{r}\frac{\partial u_z^{(q)}}{\partial \theta} + \frac{\partial u_\theta^{(q)}}{\partial z}, \end{aligned} \tag{9}$$

while the equilibrium equations per phase are written as

$$\begin{aligned} \frac{\partial \sigma_{rr}^{(q)}}{\partial r} + \frac{1}{r}\frac{\partial \sigma_{r\theta}^{(q)}}{\partial \theta} + \frac{\sigma_{rr}^{(q)} - \sigma_{\theta\theta}^{(q)}}{r} + \frac{\partial \sigma_{rz}^{(q)}}{\partial z} &= 0, \\ \frac{\partial \sigma_{r\theta}^{(q)}}{\partial r} + \frac{1}{r}\frac{\partial \sigma_{\theta\theta}^{(q)}}{\partial \theta} + \frac{2\sigma_{r\theta}^{(q)}}{r} + \frac{\partial \sigma_{\theta z}^{(q)}}{\partial z} &= 0, \\ \frac{\partial \sigma_{rz}^{(q)}}{\partial r} + \frac{1}{r}\frac{\partial \sigma_{\theta z}^{(q)}}{\partial \theta} + \frac{\sigma_{rz}^{(q)}}{r} + \frac{\partial \sigma_{zz}^{(q)}}{\partial z} &= 0. \end{aligned} \tag{10}$$

According to the RVE of Fig. 6$_a$, the fiber has radius $r = r_1$, the coating layer has external radius r_2 and the matrix has external radius r_0. In the sequel, the ratios

$$\phi_c = \frac{r_1^2}{r_2^2} = \frac{V_1}{V_1 + V_2}, \quad \phi_m = \frac{r_2^2}{r_0^2} = \frac{V_1 + V_2}{V}, \tag{11}$$

[2] Thorough discussion about the implications arising from this assumption is given in Lagoudas et al. (1991).

[3] In the sequel, the exponent $^{(q)}$ above a symbol will denote that the aforementioned quantity may vary spatially.

are introduced. Using these ratios, the volume fractions of the material constituents, c_i, are given by the expressions

$$c_1 = \phi_c\phi_m, \quad c_2 = \phi_m[1-\phi_c], \quad c_0 = 1-\phi_m. \tag{12}$$

For the heterogeneous mesoscale RVE, the traction and displacement continuity between fiber-coating and between coating-matrix are expressed through the relations

$$\begin{aligned} &u_k^{(1)}(r_1,\theta,z) = u_k^{(2)}(r_1,\theta,z), u_k^{(2)}(r_2,\theta,z) = u_k^{(0)}(r_2,\theta,z), k = r,\theta,z,\\ &\sigma_{rk}^{(1)}(r_1,\theta,z) = \sigma_{rk}^{(2)}(r_1,\theta,z), \sigma_{rk}^{(2)}(r_2,\theta,z) = \sigma_{rk}^{(0)}(r_2,\theta,z), k = r,\theta,z. \end{aligned} \tag{13}$$

Concerning the analytical homogenization strategy, average fields per phase are required to be computed. Considering the phase q, which has inner radius r_a, outer radius r_b and length $2L$, its average strain and stress, in Voigt notation, are given by the expressions

$$\begin{aligned} \boldsymbol{\varepsilon}_q &= \frac{1}{2L\pi[r_b^2-r_a^2]}\int_{-L}^{L}\int_0^{2\pi}\int_{r_a}^{r_b}\tilde{\mathbf{Q}}^T\cdot\boldsymbol{\varepsilon}^{\mathrm{cyl}(q)} r\,\mathrm{d}r\,\mathrm{d}\theta\,\mathrm{d}z,\\ \boldsymbol{\sigma}_q &= \frac{1}{2L\pi[r_b^2-r_a^2]}\int_{-L}^{L}\int_0^{2\pi}\int_{r_a}^{r_b}\tilde{\mathbf{Q}}^T\cdot\boldsymbol{\sigma}^{\mathrm{cyl}(q)} r\,\mathrm{d}r\,\mathrm{d}\theta\,\mathrm{d}z. \end{aligned} \tag{14}$$

The rotation matrices $\check{Q}$ and $\tilde{Q}$ are given in Appendix A.

A major hypothesis in the proposed method is that the equivalent medium is transversely isotropic with elasticity tensor expressed in the form

$$\bar{\boldsymbol{L}} = \begin{bmatrix} \bar{K}^{\mathrm{tr}}+\bar{\mu}^{\mathrm{tr}} & \bar{K}^{\mathrm{tr}}-\bar{\mu}^{\mathrm{tr}} & \bar{l} & 0 & 0 & 0\\ \bar{K}^{\mathrm{tr}}-\bar{\mu}^{\mathrm{tr}} & \bar{K}^{\mathrm{tr}}+\bar{\mu}^{\mathrm{tr}} & \bar{l} & 0 & 0 & 0\\ \bar{l} & \bar{l} & \bar{n} & 0 & 0 & 0\\ 0 & 0 & 0 & \bar{\mu}^{\mathrm{tr}} & 0 & 0\\ 0 & 0 & 0 & 0 & \bar{\mu}^{\mathrm{ax}} & 0\\ 0 & 0 & 0 & 0 & 0 & \bar{\mu}^{\mathrm{ax}} \end{bmatrix}.$$

The unknown material properties are the transverse bulk modulus, $\bar{K}^{\mathrm{tr}}$, the transverse shear modulus, $\bar{\mu}^{\mathrm{tr}}$, the axial shear modulus, $\bar{\mu}^{\mathrm{ax}}$, and the coefficients $\bar{l}$ and $\bar{n}$. The transverse isotropy of the overall medium has been verified in the past through the more accurate periodic homogenization framework (Chatzigeorgiou et al., 2011; Seidel et al., 2014). In the numerical example of the current article, the same conclusion is obtained.

Following the classical development of the Composite Cylinders Assemblage approach, several boundary value problems are solved analytically. The adopted strategy has the following steps:

1. Apply special macroscopic boundary conditions and inelastic stresses per phase. The analytical solutions for these conditions are known up to several constants.
2. Obtain the values of constants by using the boundary and the interface conditions between layers.
3. Compute the various concentration tensors $\boldsymbol{A}_i, \boldsymbol{A}_{j,i}^p, \boldsymbol{D}_i$ and $\boldsymbol{D}_{j,i}^p$ for i,j=0,1,2.
4. Compute the macroscopic elasticity tensor, $\bar{\boldsymbol{L}}$, and the inelastic stress concentration tensors, $\boldsymbol{B}_j^p$, using the expressions (8).

A small change in the above strategy is required for obtaining the macroscopic transverse shear modulus. In the relevant subsection, the details of this deviation are provided.

3.2. Axial shear 13

The applied displacement boundary conditions in the RVE are

$$u_z^{\mathrm{ext}}(r_0,\theta,z) = 2\beta r_0\cos\theta. \tag{15}$$

This field corresponds to the macroscopic shear angle $2\bar{\varepsilon}_{13} = 2\beta$ (Fig. 7). The three phases are subjected to inelastic stresses whose non zero components per phase are

$$\sigma_{rz}^{p(i)} = s_i\cos\theta, \quad \sigma_{\theta z}^{p(i)} = -s_i\sin\theta, \quad i = 0,1,2. \tag{16}$$

The latter corresponds to uniform shear stress on the plane x_1-x_3. The constants β, s_1, s_2 and s_0 are known. The displacement fields at every r,θ and z that satisfy the equilibrium equations (10) take the analytical forms

$$\begin{aligned} &u_r^{(1)} = u_\theta^{(1)} = 0, \quad u_z^{(1)} = r\Xi_{1,1}\cos\theta,\\ &u_r^{(2)} = u_\theta^{(2)} = 0, \quad u_z^{(2)} = r\sum_{i=1}^{2}\Xi_{2,i}\left[\frac{r}{r_1}\right]^{\xi_i-1}\cos\theta,\\ &u_r^{(0)} = u_\theta^{(0)} = 0, \quad u_z^{(0)} = r\left[\Xi_{0,1}+\Xi_{0,2}\left[\frac{r}{r_2}\right]^{-2}\right]\cos\theta, \end{aligned} \tag{17}$$

with

$$\xi_1 = \sqrt{\frac{\mu_2^{\theta z}}{\mu_2^{rz}}}, \quad \xi_2 = -\sqrt{\frac{\mu_2^{\theta z}}{\mu_2^{rz}}}. \tag{18}$$

For the expression of $u_z^{(1)}$, it has been taken into account that the displacement at $r=0$ is finite. The values of the constants $\Xi_{i,j}$ and the concentration tensors terms $A_{i_{xz}}, A_{j,i_{xz}}^p, D_{i_{xz}}$ and $D_{j,i_{xz}}^p$ for i,j=0,1,2, are determined with the procedure discussed in Section B.1 of Appendix B.

Axial shear 23 conditions follow the same procedure: The applied displacement boundary conditions in the RVE are

$$u_z^{\mathrm{ext}}(r_0,\theta,z) = 2\beta r_0\sin\theta, \tag{19}$$

which correspond to the macroscopic shear angle $2\bar{\varepsilon}_{23} = 2\beta$. The three phases are subjected to inelastic stresses whose non zero components per phase are

$$\sigma_{rz}^{p(i)} = s_i\sin\theta, \quad \sigma_{\theta z}^{p(i)} = s_i\cos\theta, \quad i = 0,1,2. \tag{20}$$

The latter corresponds to uniform shear stress on the plane x_2-x_3. The constants β, s_1, s_2 and s_0 are known. The displacement fields at every r,θ and z that satisfy the equilibrium equations (10) take similar analytical forms with the ones of the axial shear 13 case, simply by exchanging $\cos\theta$ with $\sin\theta$. Moreover, the obtained concentration tensor terms are exactly the same with those obtained in the axial shear 13 boundary value problem.

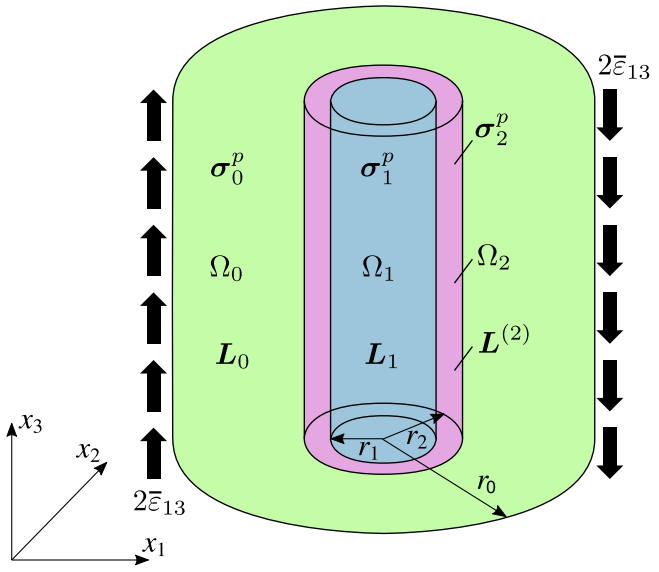

Fig. 7. Axial shear conditions.

3.3. Transverse normal conditions

The applied displacement boundary conditions in the RVE are

$$u_r^{\text{ext}}(r_0,\theta,z)=\beta r_0. \tag{21}$$

This field corresponds to the biaxial macroscopic normal strain condition $\bar{\varepsilon}_{11}=\bar{\varepsilon}_{22}=\beta$ (Fig. 8). The three phases are subjected to inelastic stresses whose non zero components per phase are

$$\sigma_{rr}^{p(i)}=\sigma_{\theta\theta}^{p(i)}=s_i,\quad i=0,1,2. \tag{22}$$

The latter corresponds to equibiaxial stress on the plane x_1-x_2. The constants β, s_1, s_2 and s_0 are known. The displacement fields at every r,θ and z that satisfy the equilibrium equations (10) take the analytical forms

$$\begin{aligned}
u_r^{(1)}&=r\Xi_{1,1}, & u_\theta^{(1)}&=u_z^{(1)}=0,\\
u_r^{(2)}&=r\sum_{i=1}^{2}\Xi_{2,i}\left[\frac{r}{r_1}\right]^{\xi_i-1}, & u_\theta^{(2)}&=u_z^{(2)}=0,\\
u_r^{(0)}&=r\left[\Xi_{0,1}+\Xi_{0,2}\left[\frac{r}{r_2}\right]^{-2}\right], & u_\theta^{(0)}&=u_z^{(0)}=0,
\end{aligned} \tag{23}$$

with

$$\xi_1=\sqrt{\frac{L_2^{\theta\theta}}{L_2^{rr}}},\quad \xi_2=-\sqrt{\frac{L_2^{\theta\theta}}{L_2^{rr}}}. \tag{24}$$

For the expression of $u_r^{(1)}$, it has been taken into account that the displacement at $r=0$ is finite. The values of the constants $\Xi_{i,j}$ and the concentration tensors terms $A_{i_{xx}}, A^p_{j,i_{xx}}, D_{i_{xx}}, D^p_{j,i_{xx}}, D_{i_{x/x}}$ and $D^p_{j,i_{x/x}}$ for i,j=0,1,2, are determined with the procedure discussed in Section B.2 of Appendix B.

3.4. Axial conditions

The applied displacement boundary conditions in the RVE are

$$u_z^{\text{ext}}(r,\theta,\pm L)=\pm\beta L,\quad u_r^{\text{ext}}(r_0,\theta,z)=0. \tag{25}$$

This field corresponds to the axial macroscopic normal strain $\bar{\varepsilon}_{33}=\beta$ (Fig. 9). The three phases are subjected to inelastic stresses whose non zero components per phase are

$$\sigma_{zz}^{p(i)}=s_i,\quad i=0,1,2. \tag{26}$$

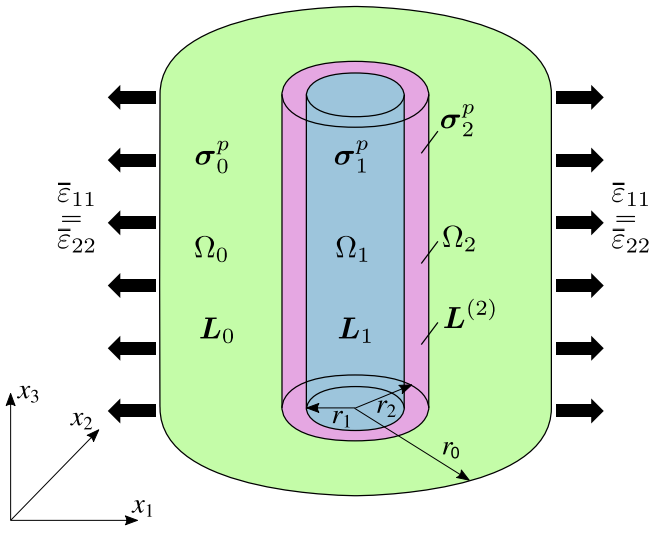

Fig. 8. Transverse normal conditions.

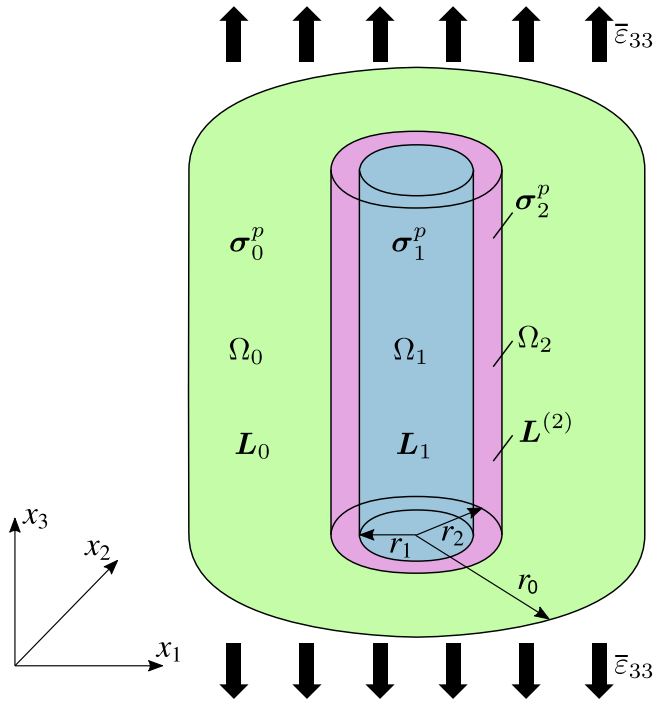

Fig. 9. Axial conditions.

The latter corresponds to axial stress in the x_3 direction. The constants β, s_1 and s_2 are known. The displacement fields at every r,θ and z that satisfy the equilibrium equations (10) take the analytical forms

$$\begin{aligned}
u_r^{(1)}&=r\Xi_{1,1}, & u_\theta^{(1)}&=0, & u_z^{(1)}&=\beta z,\\
u_r^{(2)}&=\gamma_2\beta r+r\sum_{i=1}^{2}\Xi_{2,i}\left[\frac{r}{r_1}\right]^{\xi_i-1}, & u_\theta^{(2)}&=0, & u_z^{(2)}&=\beta z,\\
u_r^{(0)}&=r\left[\Xi_{0,1}+\Xi_{0,2}\left[\frac{r}{r_2}\right]^{-2}\right], & u_\theta^{(0)}&=0, & u_z^{(0)}&=\beta z,
\end{aligned} \tag{27}$$

with

$$\gamma_2=\frac{L_2^{\theta z}-L_2^{rz}}{L_2^{rr}-L_2^{\theta\theta}},\quad \xi_1=\sqrt{\frac{L_2^{\theta\theta}}{L_2^{rr}}},\quad \xi_2=-\sqrt{\frac{L_2^{\theta\theta}}{L_2^{rr}}}. \tag{28}$$

For the expression of $u_r^{(1)}$, it has been taken into account that the displacement at $r=0$ is finite. The values of the constants $\Xi_{i,j}$ and the concentration tensors terms $A_{i_{x-z}}, D_{i_{x-z}}$ and D_{i_z} for i,j=0,1,2, are determined with the procedure discussed in Section B.3 of Appendix B.

3.5. Transverse shear conditions

Following Christensen and Lo (1979), the Generalized Self Consistent Composite Cylinders Assemblage strategy is considered for this case. The traction boundary conditions are:

$$\sigma_{rr}^{\text{ext}}(r_{\text{ext}},\theta,z)=\beta\sin 2\theta,\quad \sigma_{r\theta}^{\text{ext}}(r_{\text{ext}},\theta,z)=\beta\cos 2\theta,\quad r_{\text{ext}}\to\infty. \tag{29}$$

These conditions correspond to macroscopic transverse shear stress $\bar{\sigma}_{12}$. A fourth layer is added to the RVE, which is characterized by the unknown material properties $\bar{\boldsymbol{L}}$ (Fig. 10). The four phases are subjected to inelastic stresses whose non zero components per phase are

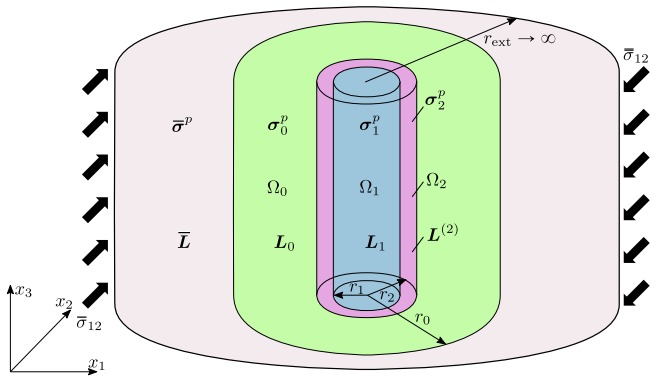

Fig. 10. Four cylinders RVE model used in the generalized self consistent approach and transverse shear conditions.

$$\begin{aligned}&\sigma_{rr}^{p(i)} = s_i \sin 2\theta, \sigma_{\theta\theta}^{p(i)} = -s_i \sin 2\theta, \sigma_{r\theta}^{p(i)} = s_i \cos 2\theta, \quad i = 0,1,2,\\ &\sigma_{rr}^{p(3)} = \bar{s} \sin 2\theta, \sigma_{\theta\theta}^{p(3)} = -\bar{s} \sin 2\theta, \sigma_{r\theta}^{p(3)} = \bar{s} \cos 2\theta.\end{aligned} \tag{30}$$

The latter correspond to transverse inelastic shear stresses on the plane $x_1 - x_2$. $\bar{s}$ is the unknown macroscopic inelastic stress. The traction and displacement continuity between the matrix and the equivalent medium are expressed through the relations

$$u_k^{(0)}(r_0,\theta,z) = u_k^{(3)}(r_0,\theta,z), \quad \sigma_{rk}^{(0)}(r_0,\theta,z) = \sigma_{rk}^{(3)}(r_0,\theta,z), \quad k = r,\theta,z. \tag{31}$$

The constants β, s_1, s_2 and s_0 are known. The nonzero displacement fields at every r, θ and z that satisfy the equilibrium equations (10) and the boundary conditions take the analytical forms

$$\begin{aligned}u_r^{(1)} &= r\left[Z_1 \Xi_{1,1}\left[\frac{r}{r_1}\right]^2 + \Xi_{1,2}\right]\sin 2\theta,\\ u_\theta^{(1)} &= r\left[\Xi_{1,1}\left[\frac{r}{r_1}\right]^2 + \Xi_{1,2}\right]\cos 2\theta,\end{aligned} \tag{32}$$

$$\begin{aligned}u_r^{(2)} &= r\left[\sum_{i=1}^{4} X_i \Xi_{2,i}\left[\frac{r}{r_1}\right]^{\xi_i - 1}\right]\sin 2\theta,\\ u_\theta^{(2)} &= r\left[\sum_{i=1}^{4} \Xi_{2,i}\left[\frac{r}{r_1}\right]^{\xi_i - 1}\right]\cos 2\theta,\end{aligned} \tag{33}$$

$$\begin{aligned}u_r^{(0)} &= r\left[Z_0 \Xi_{0,1}\left[\frac{r}{r_2}\right]^2 + \Xi_{0,2} - \Xi_{0,3}\left[\frac{r}{r_2}\right]^{-4} + Z\prime_0 \Xi_{0,4}\left[\frac{r}{r_2}\right]^{-2}\right]\sin 2\theta,\\ u_\theta^{(0)} &= r\left[\Xi_{0,1}\left[\frac{r}{r_2}\right]^2 + \Xi_{0,2} + \Xi_{0,3}\left[\frac{r}{r_2}\right]^{-4} + \Xi_{0,4}\left[\frac{r}{r_2}\right]^{-2}\right]\cos 2\theta,\end{aligned} \tag{34}$$

$$\begin{aligned}u_r^{(3)} &= \frac{r}{2\bar{\mu}^{tr}}\left[\beta - \bar{\Xi}_3\left[\frac{r}{r_0}\right]^{-4} + \bar{Z}\prime \bar{\Xi}_4\left[\frac{r}{r_0}\right]^{-2}\right]\sin 2\theta,\\ u_\theta^{(3)} &= \frac{r}{2\bar{\mu}^{tr}}\left[\beta + \bar{\Xi}_3\left[\frac{r}{r_0}\right]^{-4} + \bar{\Xi}_4\left[\frac{r}{r_0}\right]^{-2}\right]\cos 2\theta.\end{aligned} \tag{35}$$

In the above expressions,

$$\begin{aligned}&Z_1 = \frac{K_1^{tr} - \mu_1^{tr}}{2K_1^{tr} + \mu_1^{tr}}, \quad Z_0 = \frac{K_0^{tr} - \mu_0^{tr}}{2K_0^{tr} + \mu_0^{tr}},\\ &Z_0' = \frac{K_0^{tr} + \mu_0^{tr}}{\mu_0^{tr}}, \quad \bar{Z}' = \frac{\bar{K}^{tr} + \bar{\mu}^{tr}}{\bar{\mu}^{tr}},\end{aligned} \tag{36}$$

and

$$X_i = 2\frac{L_2^{\theta\theta} - \xi_i L_2^{r\theta} + [1 - \xi_i]\mu_2^{r\theta}}{L_2^{\theta\theta} + 4\mu_2^{r\theta} - L_2^{rr}\xi_i^2}, \quad i = 1,2,3,4. \tag{37}$$

Moreover, ξ_i are the four solutions of the following polynomial equation:

$$9L_2^{\theta\theta}\mu_2^{r\theta} + L_2^{rr}\mu_2^{r\theta}\xi_i^4 + \left[4L_2^{r\theta}[L_2^{r\theta} + 2\mu_2^{r\theta}] - L_2^{\theta\theta}\mu_2^{r\theta} - L_2^{rr}[4L_2^{\theta\theta} + \mu_2^{r\theta}]\right]\xi_i^2 = 0. \tag{38}$$

The values of the constants $\Xi_{i,j}$ and the concentration tensors terms $A_{i_{xy}}, A_{j,i_{xy}}^p, D_{i_{xy}}$ and $D_{j,i_{xy}}^p$ for i,j=0,1,2, are determined with the procedure discussed in Section B.4 of Appendix B.

3.6. Deviatoric conditions

This case is similar with the previous one. The applied traction boundary conditions are:

$$\begin{aligned}\sigma_{rr}^{ext}(r_{ext},\theta,z) &= \beta\cos 2\theta,\\ \sigma_{\theta\theta}^{ext}(r_{ext},\theta,z) &= -\beta\cos 2\theta,\\ \sigma_{r\theta}^{ext}(r_{ext},\theta,z) &= -\beta\sin 2\theta, \quad r_{ext} \to \infty.\end{aligned} \tag{39}$$

Once again, a fourth layer is added to the RVE, which is characterized by the unknown material properties $\bar{\boldsymbol{L}}$. The four phases are subjected to inelastic stresses whose non zero components per phase are

$$\begin{aligned}&\sigma_{rr}^{p(i)} = s_i \cos\theta, \sigma_{\theta\theta}^{p(i)} = -s_i \cos 2\theta, \sigma_{r\theta}^{p(i)} = -s_i \sin 2\theta, \quad i = 0,1,2,\\ &\sigma_{rr}^{p(3)} = \bar{s} \cos 2\theta, \sigma_{\theta\theta}^{p(3)} = -\bar{s} \cos 2\theta, \sigma_{r\theta}^{p(3)} = -\bar{s} \sin 2\theta,\end{aligned} \tag{40}$$

where $\bar{s}$ is the unknown macroscopic inelastic stress. The deviatoric conditions lead to similar solution with the transverse shear conditions. The displacement fields in all phases are expressed in the general form[4]

$$\begin{aligned}u_r &= r\left[\sum_{i=1}^{4} X_i \Xi_i\left[\frac{r}{r_1}\right]^{\xi_i - 1}\right]\cos 2\theta,\\ u_\theta &= -r\left[\sum_{i=1}^{4} \Xi_i\left[\frac{r}{r_1}\right]^{\xi_i - 1}\right]\sin 2\theta.\end{aligned} \tag{41}$$

Some computational details for this boundary value problem are given in Section B.5 of Appendix B.

3.7. Concentration tensors

The obtained concentration tensor terms from the previously discussed boundary value problems are sufficient to establish the complete form of the tensors. Indeed, in Voigt notation they are written as

$$\boldsymbol{A}_i = \begin{bmatrix} \frac{A_{i_{xx}} + A_{i_{xy}}}{2} & \frac{A_{i_{xx}} - A_{i_{xy}}}{2} & A_{i_{x-z}} & 0 & 0 & 0\\ \frac{A_{i_{xx}} - A_{i_{xy}}}{2} & \frac{A_{i_{xx}} + A_{i_{xy}}}{2} & A_{i_{x-z}} & 0 & 0 & 0\\ 0 & 0 & 1 & 0 & 0 & 0\\ 0 & 0 & 0 & A_{i_{xy}} & 0 & 0\\ 0 & 0 & 0 & 0 & A_{i_{xz}} & 0\\ 0 & 0 & 0 & 0 & 0 & A_{i_{xz}} \end{bmatrix}, \tag{42}$$

[4] Some terms vanish in certain phases, see the previous boundary value problem.

$$\boldsymbol{A}^{p}_{j,i}=\begin{bmatrix} \frac{A^{p}_{j,i_{xx}}+A^{p}_{j,i_{xy}}/2}{2} & \frac{A^{p}_{j,i_{xx}}-A^{p}_{j,i_{xy}}/2}{2} & 0 & 0 & 0 & 0 \\ \frac{A^{p}_{j,i_{xx}}-A^{p}_{j,i_{xy}}/2}{2} & \frac{A^{p}_{j,i_{xx}}+A^{p}_{j,i_{xy}}/2}{2} & 0 & 0 & 0 & 0 \\ 0 & 0 & 0 & 0 & 0 & 0 \\ 0 & 0 & 0 & A^{p}_{j,i_{xy}} & 0 & 0 \\ 0 & 0 & 0 & 0 & A^{p}_{j,i_{xz}} & 0 \\ 0 & 0 & 0 & 0 & 0 & A^{p}_{j,i_{xz}} \end{bmatrix}, \tag{43}$$

$$\boldsymbol{D}_{i}=\begin{bmatrix} \frac{D_{i_{xx}}+2D_{i_{xy}}}{2} & \frac{D_{i_{xx}}-2D_{i_{xy}}}{2} & D_{i_{x-z}} & 0 & 0 & 0 \\ \frac{D_{i_{xx}}-2D_{i_{xy}}}{2} & \frac{D_{i_{xx}}+2D_{i_{xy}}}{2} & D_{i_{x-z}} & 0 & 0 & 0 \\ \frac{D_{i_{x/x}}}{2} & \frac{D_{i_{x/x}}}{2} & D_{i_{z}} & 0 & 0 & 0 \\ 0 & 0 & 0 & D_{i_{xy}} & 0 & 0 \\ 0 & 0 & 0 & 0 & D_{i_{xz}} & 0 \\ 0 & 0 & 0 & 0 & 0 & D_{i_{xz}} \end{bmatrix}, \tag{44}$$

and

$$\boldsymbol{D}^{p}_{j,i}=\begin{bmatrix} \frac{D^{p}_{j,i_{xx}}+D^{p}_{j,i_{xy}}}{2} & \frac{D^{p}_{j,i_{xx}}-D^{p}_{j,i_{xy}}}{2} & 0 & 0 & 0 & 0 \\ \frac{D^{p}_{j,i_{xx}}-D^{p}_{j,i_{xy}}}{2} & \frac{D^{p}_{j,i_{xx}}+D^{p}_{j,i_{xy}}}{2} & 0 & 0 & 0 & 0 \\ \frac{D^{p}_{j,i_{x/x}}}{2} & \frac{D^{p}_{j,i_{x/x}}}{2} & \delta_{ji} & 0 & 0 & 0 \\ 0 & 0 & 0 & D^{p}_{j,i_{xy}} & 0 & 0 \\ 0 & 0 & 0 & 0 & D^{p}_{j,i_{xz}} & 0 \\ 0 & 0 & 0 & 0 & 0 & D^{p}_{j,i_{xz}} \end{bmatrix}, \tag{45}$$

for i,j=0,1,2. All the constants of the above tensors are obtained through the procedure described in the Appendix B. δ_{ji} stands for the Kronecker delta symbol, given in Eq. (B.1).

3.8. Thermal conditions

When a fuzzy fiber composite is subjected to thermal conditions, the nanocomposite experiences thermal stresses which are constant in the cylindrical coordinate system. The thermal stress tensor is known, since it depends on material properties (elasticity and thermal conductivity tensors), and it takes the form

$$\boldsymbol{\sigma}_{2}^{\text{thcyl}}=\begin{bmatrix} s_{2}^{r} & s_{2}^{\theta} & s_{2}^{z} & 0 & 0 & 0 \end{bmatrix}^{T},$$

where, in general, $s_2^r \neq s_2^\theta \neq s_2^z$. Transforming $\boldsymbol{\sigma}_2^{\text{thcyl}}$ to Cartesian coordinates produces a spatially dependent $\boldsymbol{\sigma}_2^{\text{th}}$, which is incompatible with the main hypothesis (2) for the constitutive law. To address this incompatibility for the thermal conditions, the following boundary value problem is studied separately from the previously examined cases: The three phases of Fig. 6$_a$ are subjected to inelastic stresses whose non zero components per phase are

$$\begin{aligned} &\sigma_{rr}^{\text{th}(1)}=\sigma_{\theta\theta}^{\text{th}(1)}=s_1^{\text{tr}}, \quad \sigma_{zz}^{\text{th}(1)}=s_1^{\text{ax}},\\ &\sigma_{rr}^{\text{th}(2)}=s_2^{r}, \quad \sigma_{\theta\theta}^{\text{th}(2)}=s_2^{\theta}, \quad \sigma_{zz}^{\text{th}(2)}=s_2^{z},\\ &\sigma_{rr}^{\text{th}(0)}=\sigma_{\theta\theta}^{\text{th}(0)}=s_0^{\text{tr}}, \quad \sigma_{zz}^{\text{th}(0)}=s_0^{\text{ax}}. \end{aligned} \tag{46}$$

The displacement fields at every r,θ and z that satisfy the equilibrium equations take the analytical forms

$$\begin{aligned} &u_r^{(1)}=r\Xi_{1,1}, && u_\theta^{(1)}=u_z^{(1)}=0,\\ &u_r^{(2)}=rX[s_2^r-s_2^\theta]+r\sum_{i=1}^{2}\Xi_{2,i}\left[\frac{r}{r_1}\right]^{\xi_i-1}, && u_\theta^{(2)}=u_z^{(2)}=0,\\ &u_r^{(0)}=r\left[\Xi_{0,1}+\Xi_{0,2}\left[\frac{r}{r_2}\right]^{-2}\right], && u_\theta^{(0)}=u_z^{(0)}=0, \end{aligned} \tag{47}$$

with

$$\xi_1=\sqrt{\frac{L_2^{\theta\theta}}{L_2^{rr}}}, \quad \xi_2=-\sqrt{\frac{L_2^{\theta\theta}}{L_2^{rr}}}, \quad X=\frac{1}{L_2^{\theta\theta}-L_2^{rr}}. \tag{48}$$

For the expression of $u_r^{(1)}$, it has been taken into account that the displacement at $r=0$ is finite. The computational details for obtaining the macroscopic thermal stress tensor, $\bar{\boldsymbol{\sigma}}^{\text{th}}$, are provided in Section B.6 of Appendix B.

4. Numerical example

This section presents a numerical example of a fuzzy fiber composite with wavy carbon nanotubes. The scope is to investigate the accuracy of the proposed methodology. In a forthcoming article, a proper parametric investigation and applications in nonlinear composites will demonstrate the method's efficiency.

4.1. Material properties and geometrical characteristics

Concerning the material phases, the matrix is assumed to be a typical epoxy; the main fibers are made of glass and the carbon nanotubes walls are made of graphene. All these materials are isotropic and their properties are summarized in Table 1. While the graphene is considered isotropic, it should be noted that the effective behavior of a CNT, single-walled or multi-walled, is anisotropic. Straight CNTs behave as transversely isotropic effective media and their properties can be obtained through micromechanical techniques (Seidel and Lagoudas, 2006).

With regard to the microscale, the CNTs (hollow microfibers made of graphene) have internal radius 0.51 nm, external radius 0.85 nm (Chatzigeorgiou et al., 2012). The wavy geometric characteristics of the CNT and its position inside the microscale RVE is illustrated in Fig. 11. The width per length ratio of the RVE is considered equal to 1/4, while the waviness of the CNT (height per length) is taken equal to 0.1. The CNTs are wavy in the $r-\theta$ space, they appear in tetragonal arrangement inside the nanocomposite, and their overall volume fraction in the nanocomposite is 10%.

With regard to the mesoscale, the glass fiber radius is taken equal to 2.5 μm, the length of the CNTs (i.e. thickness of nanocom-

Table 1
Material properties of fuzzy fiber composite constituents. The mechanical properties of graphene have been obtained from Chatzigeorgiou et al. (2012), while the thermal from Shaina et al. (2016).

Property	Epoxy	Glass	Graphene
Young's Modulus [MPa]	3000	72000	1100000
Poisson's ratio	0.3	0.2	0.14
Thermal expansion coefficient [1/K]	1.1E−4	5.0E−6	−3.75E−6

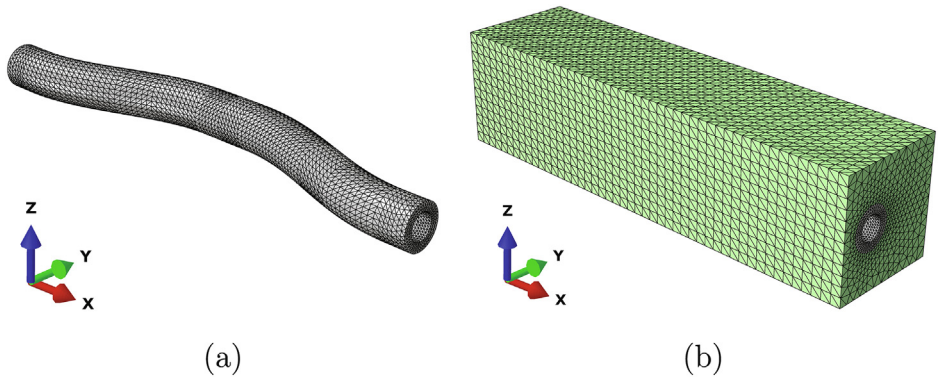

Fig. 11. (a) Wavy CNT and (b) RVE at the microscopic scale with tetragonal arrangement of CNTs.

Table 2
Thermomechanical properties of the nanocomposite obtained via periodic homogenization.

Property	Value	Property	Value
L_2^{rr} [MPa]	34420.2	$\mu_2^{r\theta}$ [MPa]	1575.0
$L_2^{r\theta}$ [MPa]	2568.0	μ_2^{rz} [MPa]	1416.2
L_2^{rz} [MPa]	1940.5	$\mu_2^{\theta z}$ [MPa]	1349.4
$L_2^{\theta\theta}$ [MPa]	4779.5	σ_2^{thr} [MPa/K]	−0.6784
$L_2^{\theta z}$ [MPa]	1967.6	$\sigma_2^{\mathrm{th}\theta}$ [MPa/K]	−0.8161
L_2^{zz} [MPa]	4712.8	σ_2^{thz} [MPa/K]	−0.8193

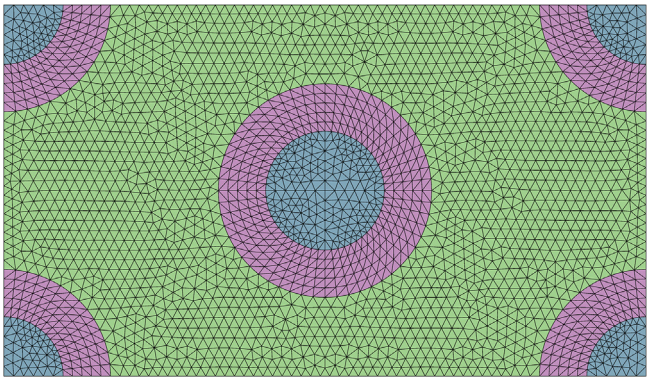

Fig. 12. Mesoscopic RVE of the fuzzy fiber composite according to the periodic homogenization strategy. The fuzzy fibers appear with hexagonal arrangement.

posite) is equal to 2 μm, and the fuzzy fiber's overall volume fraction in the composite is taken equal to 30%.

4.2. Microscale homogenization: effective response of nanocomposite

The microscale RVE is solved with the help of the FE software ABAQUS. Periodicity conditions are imposed at the boundaries of the RVE and the mesoscopic strain is provided with the help of the constraint drivers concept (Praud, 2018; Tikarrouchine et al., 2018). Six linear perturbation analyses are performed to establish the complete elasticity tensor of the nanocomposite. For the thermal stresses, zero mesoscopic strain and unit temperature are applied at the constraint drivers (Tikarrouchine et al., 2019). The FE computations have been performed using 150088 fully integrated ten-node tetrahedral elements (C3D10). The nanocomposite properties from this analysis are summarized in Table 2. The effective thermal expansion coefficients tensor, $\boldsymbol{\alpha}_2$, can be computed by the classical relation

$$\boldsymbol{\alpha}_2^{\mathrm{cyl}} = -\left[\boldsymbol{L}_2^{\mathrm{cyl}}\right]^{-1} : \boldsymbol{\sigma}_2^{\mathrm{thcyl}}.$$

Table 3
Thermomechanical properties of the fuzzy fiber composite. Results obtained via periodic homogenization (PH) and CCA and relative error of CCA.

Property	PH	CCA	Error
$\bar{K}^{\mathrm{tr}}$ [MPa]	4185.5	4184.4	0.03%
$\bar{l}$ [MPa]	2025.0	2024.8	0.01%
$\bar{n}$ [MPa]	10630.5	10626.2	0.04%
$\bar{\mu}^{\mathrm{tr}}$ [MPa]	1616.3	1629.7	0.83%
$\bar{\mu}^{\mathrm{ax}}$ [MPa]	1442.1	1441.9	0.01%
$\bar{\sigma}^{\mathrm{thtr}}$ [MPa/K]	−0.8161	−0.8161	0.00%
$\bar{\sigma}^{\mathrm{thax}}$ [MPa/K]	−0.8097	−0.8097	0.00%

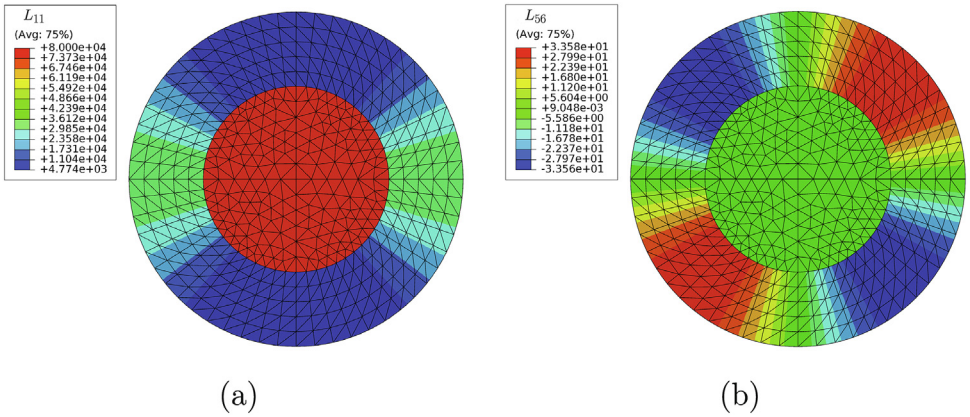

Fig. 13. Spatial distribution of (a) L_{11} and (b) L_{56} component in the glass fiber and the nanocomposite.

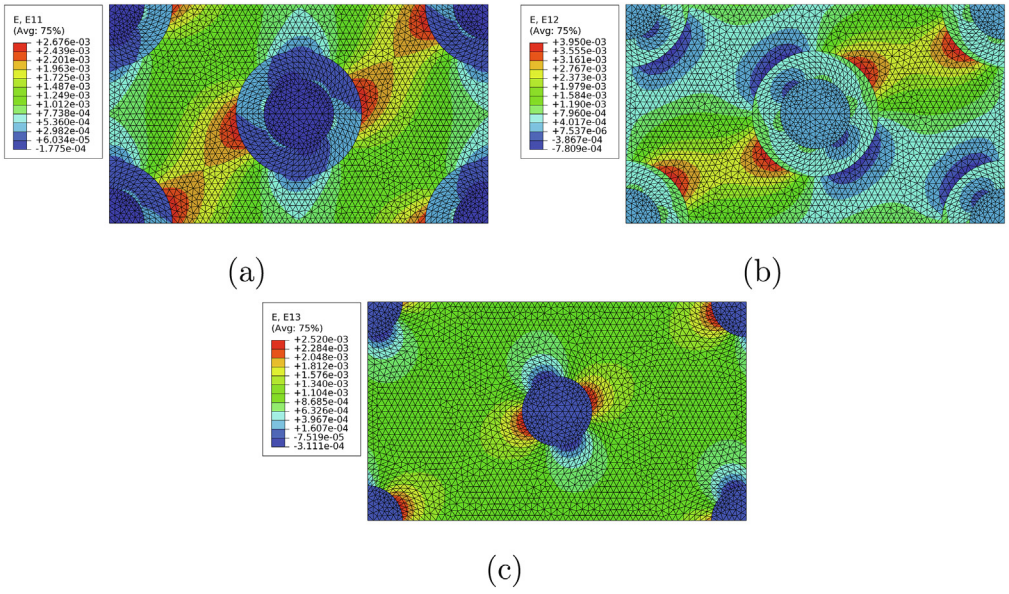

Fig. 14. Distribution of strains in the mesoscale RVE: (a) 11 normal strain, (b) 12 shear angle and (c) 13 shear angle.

Table 4
Macroscopic inelastic stresses obtained via periodic homogenization (PH) and CCA and relative error of CCA. The stress components units are in MPa.

	$\bar{\sigma}_{11}$	$\bar{\sigma}_{22}$	$\bar{\sigma}_{33}$	$\bar{\sigma}_{44}$	$\bar{\sigma}_{55}$	$\bar{\sigma}_{66}$
PH	10.3629	10.3631	14.5687	1.5660	1.3553	1.3554
CCA	10.3605	10.3605	14.5640	1.5785	1.3552	1.3552
Error	0.02%	0.02%	0.03%	0.80%	0.01%	0.01%

Table 5
Average strains in the fiber, the nanocomposite (NCP) and the matrix. Results are obtained via periodic homogenization (PH) and CCA.

		ε_{11}	ε_{22}	ε_{33}	ε_{44}	ε_{55}	ε_{66}
fiber	PH	1.92E−6	1.94E−6	1.00E−3	1.13E−4	1.06E−4	1.06E−4
	CCA	1.89E−6	1.89E−6	1.00E−3	1.16E−4	1.06E−4	1.06E−4
	Error	1.74%	2.44%	0.00%	2.41%	0.01%	0.01%
NCP	PH	2.50E−4	2.51E−4	1.00E−3	6.29E−4	1.10E−3	1.10E−3
	CCA	2.50E−4	2.50E−4	1.00E−3	6.37E−4	1.10E−3	1.10E−3
	Error	0.01%	0.04%	0.00%	1.26%	0.00%	0.01%
matrix	PH	1.35E−3	1.35E−3	1.00E−3	1.23E−3	1.09E−3	1.09E−3
	CCA	1.35E−3	1.35E−3	1.00E−3	1.22E−3	1.09E−3	1.09E−3
	Error	0.02%	0.02%	0.00%	0.24%	0.01%	0.01%

4.3. Mesoscale homogenization: thermomechanical properties of fuzzy fiber composite

The mesoscale RVE is solved following two different approaches: (i) via periodic homogenization and (ii) via the CCA method proposed in the previous section. The periodic homogenization, as a full-field approach, is considered to be more accurate and thus it is used here as the reference solution.

With respect to the periodic homogenization strategy, the nanocomposite properties obtained from the previous analysis are introduced in the RVE of Fig. 12. This RVE consists of matrix and fuzzy fibers distributed in hexagonal arrangement. As Fig. 13 shows, the cylindrically orthotropic nanocomposite is "translated" in the coordinate system of the mesoscale RVE as a functionally graded monoclinic medium. Its material properties depend on the angular position. Due to this spatial dependency, the constitutive law of the nanocomposite is introduced in the FE software ABAQUS with the help of an appropriate user material (UMAT) subroutine. The performed analysis is 3-D, since though the composite is unidirectional, only one element in the x_3 direction is sufficient for accurate results. The FE computations have been performed using 16552 fully integrated ten-node tetrahedral elements (C3D10). The obtained results have been validated with performed analyses using two different meshes, one coarser (7391 C3D10 elements) and one finer (84787 C3D10 elements) than the chosen mesh in the present study.

In the same spirit with the microscale analysis, periodicity conditions are imposed at the boundaries of the mesoscale RVE and the macroscopic strain is provided with the help of the constraint drivers concept. For the thermal stresses, zero macroscopic strain and unit temperature are applied at the constraint drivers.

Table 3 summarizes the results obtained from the periodic homogenization and from the CCA method as described in the previous section. The relative error for each property is the absolute value of the difference between the results of the two methods, divided by the value given by the periodic homogenization. The first observation is that the periodic homogenization results provide transversely isotropic response of the composite[5]. The second observation is that the CCA method provides very accurate predic-

[5] Slight deviations in second and third digits are due to the numerical accuracy of the FE computations and inherent trancatures.

Table 6
Average stresses in the fiber, the nanocomposite (NCP) and the matrix. Results are obtained via periodic homogenization (PH) and CCA. The stress components units are in MPa.

		σ_{11}	σ_{22}	σ_{33}	σ_{44}	σ_{55}	σ_{66}
fiber	PH	19.5924	19.5932	79.4771	2.7939	2.5880	2.5881
	CCA	19.5888	19.5888	79.4755	2.8756	2.5878	2.5878
	Error	0.02%	0.02%	0.00%	2.92%	0.01%	0.01%
NCP	PH	9.0002	9.0010	5.2883	1.5229	1.1448	1.1449
	CCA	8.9987	8.9987	5.2880	1.5587	1.1447	1.1447
	Error	0.02%	0.02%	0.01%	2.35%	0.00%	0.01%
matrix	PH	9.5451	9.5451	8.7272	1.4162	1.2546	1.2546
	CCA	9.5434	9.5434	8.7262	1.4128	1.2545	1.2545
	Error	0.02%	0.02%	0.01%	0.24%	0.01%	0.01%

tions. Its biggest deviation from the periodic homogenization results (0.8%) is observed in the transverse shear component, which has been obtained via the generalized self consistent composite cylinders methodology. This observation was expected, since similar discrepancy between mean field and full field predictions has been frequently observed in the case of regular unidirectional fiber composites with moderate and high volume fraction of fibers (Hyer and Waas, 2000). The main reason for this discrepancy is that transverse shear loading leads to strain profiles inside the RVE that cannot be properly captured using the assumption of a single strain tensor per phase.

4.4. Mesoscale homogenization: fuzzy fiber composite response under macroscopic strain and inelastic fields

To test the accuracy of the concentration tensors obtained from the analytical methodology of the previous section, an additional comparison between the CCA and the periodic homogenization is provided below.

In the following example, the glass fiber and the nanocomposite are subjected to the uniform inelastic stresses

$$\boldsymbol{\sigma}_1^p = -0.6 \cdot [1 \quad 1 \quad 1 \quad 1 \quad 1 \quad 1]^T \quad \text{MPa},$$
$$\boldsymbol{\sigma}_2^p = -0.4 \cdot [1 \quad 1 \quad 1 \quad 1 \quad 1 \quad 1]^T \quad \text{MPa}.$$

The matrix is assumed to be free from inelastic stresses. In addition, the macroscopic strain

$$\bar{\boldsymbol{\varepsilon}} = 0.001 \cdot [1 \quad 1 \quad 1 \quad 1 \quad 1 \quad 1]^T,$$

is applied in the mesoscale RVE.

The uniform inelastic stresses for both the glass fiber and the nanocomposite are introduced in the FE periodic homogenization computations with the help of specially designed user material (UMAT) subroutines for the ABAQUS software. Moreover, the total macroscopic strain is applied at the constraint drivers. The distribution of the strains in the RVE from the periodic homogenization computations is illustrated in Fig. 14.

The obtained macroscopic stresses, as well as the average strains and stresses per phase are summarized in Tables 4–6, respectively. Again, it is observed an excellent agreement between the CCA and the periodic homogenization. The maximum deviation in the macroscopic and the average fields between the finite element simulations and the analytical model computations is observed in the transverse components. This phenomenon is due to the same reasons that cause deviation in the transverse shear modulus predictions, i.e. the difficulty of the mean field techniques to capture properly the strain profiles in the RVE under transverse shearing at moderate and high fiber volume fractions.

5. Conclusions

This manuscript has presented a micromechanical framework for identifying the overall response of a fuzzy fiber composite. The main novelties of the developed approach are: i) it is applicable for fibers coated with straight or wavy carbon nanotubes, and ii) it accounts for inelastic mechanical and thermal fields. The proposed method for the mesoscale problem of the composite computes strain-type and stress-type concentration tensors through the CCA approach. The inelastic fields are taken into account via the TFA strategy. A numerical example of a fuzzy fiber composite with wavy nanotubes and comparisons with full field (periodic homogenization) computations illustrates the excellent accuracy of the micromechanical founded approach.

The developed strategy has considered one set of properties to describe the overall behavior of the nanocomposite layer. In the presence of wavy CNTs, this nanocomposite behaves as a cylindrically orthotropic medium. The proposed methodology can be easily extended to express the response of the nanocomposite with more than one layers, as it is the case for the approximate locally periodic homogenization strategy. This extension could allow to combine, in the future, the CCA approach with other methods at the microscopic scale (Tsalis et al., 2012).

The present manuscript focuses on establishing a new micromechanical framework for fuzzy fiber composites. The numerical example has been utilized to validate the approach. In a forthcoming paper, a proper parametric investigation with several fuzzy fiber configurations and specific applications in nonlinear composites will demonstrate the capabilities and potential applications of the proposed method.

Declaration of Competing Interest

The authors declare that they have no known competing financial interests or personal relationships that could have appeared to influence the work reported in this paper.

Appendix A. Transformation between coordinate systems

In Voigt notation, strains and stresses are represented as 6×1 vectors. The displacement, strain and stress fields are transformed between cylindrical and Cartesian coordinate systems through the matrix-type formulas

$$\boldsymbol{u}^{\text{cyl}} = \boldsymbol{R}^T \cdot \boldsymbol{u}, \quad \boldsymbol{\varepsilon}^{\text{cyl}} = -\tilde{\mathrm{Q}} \cdot \boldsymbol{\varepsilon}, \quad \boldsymbol{\sigma}^{\text{cyl}} = -\tilde{\mathrm{Q}} \cdot \boldsymbol{\sigma},$$
$$\boldsymbol{u} = \boldsymbol{R} \cdot \boldsymbol{u}^{\text{cyl}}, \quad \boldsymbol{\varepsilon} = -\tilde{\mathrm{Q}}^T \cdot \boldsymbol{\varepsilon}^{\text{cyl}}, \quad \boldsymbol{\sigma} = -\tilde{\mathrm{Q}}^T \cdot \boldsymbol{\sigma}^{\text{cyl}},$$

where $\boldsymbol{R}$ is the rotator second order tensor

$$\boldsymbol{R} = \begin{bmatrix} \cos\theta & -\sin\theta & 0 \\ \sin\theta & \cos\theta & 0 \\ 0 & 0 & 1 \end{bmatrix}.$$

and $\tilde{\mathrm{Q}}, \check{\mathrm{Q}}$ are proper fourth order rotators that transform second order tensors in Voigt notation (Chatzigeorgiou et al., 2018),

$$\tilde{Q}=\begin{bmatrix} \cos^2\theta & \sin^2\theta & 0 & \cos\theta\sin\theta & 0 & 0\\ \sin^2\theta & \cos^2\theta & 0 & -\cos\theta\sin\theta & 0 & 0\\ 0 & 0 & 1 & 0 & 0 & 0\\ -2\cos\theta\sin\theta & 2\cos\theta\sin\theta & 0 & \cos^2\theta-\sin^2\theta & 0 & 0\\ 0 & 0 & 0 & 0 & \cos\theta & \sin\theta\\ 0 & 0 & 0 & 0 & -\sin\theta & \cos\theta \end{bmatrix},$$

$$\check{Q}=\begin{bmatrix} \cos^2\theta & \sin^2\theta & 0 & 2\cos\theta\sin\theta & 0 & 0\\ \sin^2\theta & \cos^2\theta & 0 & -2\cos\theta\sin\theta & 0 & 0\\ 0 & 0 & 1 & 0 & 0 & 0\\ -\cos\theta\sin\theta & \cos\theta\sin\theta & 0 & \cos^2\theta-\sin^2\theta & 0 & 0\\ 0 & 0 & 0 & 0 & \cos\theta & \sin\theta\\ 0 & 0 & 0 & 0 & -\sin\theta & \cos\theta \end{bmatrix}.$$

With the help of the above rotators, the transformation of a stiffness tensor $\boldsymbol{L}$ takes the form

$$\boldsymbol{L}^{\text{cyl}}=-\check{Q}\cdot\boldsymbol{L}\cdot-\check{Q}^T,\quad \boldsymbol{L}=-\tilde{Q}^T\cdot\boldsymbol{L}^{\text{cyl}}\cdot-\tilde{Q}.$$

Appendix B. Computational details for the mesoscale boundary value problems

This appendix is devoted to the presentation of the computational details for the boundary value problems discussed in Section 3. The symbol δ_{ji} that appears in the sequel denotes the Kronecker delta:

$$\delta_{ji}=\begin{cases}1, & i=j,\\ 0, & i\neq j,\end{cases}\quad i,j=0,1,2. \tag{B.1}$$

B.1. Axial shear xz

For the fields presented in Section 3.2, the average strains and stresses at every phase are given by the formulas

$$\begin{aligned}
&\boldsymbol{\varepsilon}_1=\Xi_{1,1}\boldsymbol{I}_{xz},\\
&\boldsymbol{\varepsilon}_2=\sum_{i=1}^{2}\Phi_i\Xi_{2,i}\boldsymbol{I}_{xz},\\
&\boldsymbol{\varepsilon}_0=\Xi_{0,1}\boldsymbol{I}_{xz},\\
&\boldsymbol{\sigma}_1=\left[s_1+\mu_1^{\text{ax}}\Xi_{1,1}\right]\boldsymbol{I}_{xz},\\
&\boldsymbol{\sigma}_2=\left[s_2+\mu_2^{rz}\sum_{j=1}^{2}\xi_j\Phi_j\Xi_{2,j}\right]\boldsymbol{I}_{xz},\\
&\boldsymbol{\sigma}_0=\left[s_0+\mu_0^{\text{ax}}\Xi_{0,1}\right]\boldsymbol{I}_{xz},
\end{aligned} \tag{B.2}$$

with

$$\boldsymbol{I}_{xz}=[0\quad 0\quad 0\quad 0\quad 1\quad 0]^T, \tag{B.3}$$

and

$$\Phi_i=\frac{\sqrt{\phi_c}^{1-\xi_i}-\phi_c}{1-\phi_c}. \tag{B.4}$$

Using the interface and boundary conditions one obtains the linear system

$$\boldsymbol{K}\cdot\boldsymbol{\Xi}=2\beta\boldsymbol{F}_\beta+\sum_{i=0}^{2}s_i\boldsymbol{F}_i, \tag{B.5}$$

where

$$\begin{aligned}
\boldsymbol{\Xi}&=[\Xi_{1,1}\quad \Xi_{2,1}\quad \Xi_{2,2}\quad \Xi_{0,1}\quad \Xi_{0,2}]^T,\\
\boldsymbol{F}_\beta&=[0\quad 0\quad 0\quad 0\quad 1]^T,\\
\boldsymbol{F}_1&=[0\quad -1\quad 0\quad 0\quad 0]^T,\\
\boldsymbol{F}_2&=[0\quad 1\quad 0\quad -1\quad 0]^T,\\
\boldsymbol{F}_0&=[0\quad 0\quad 0\quad 1\quad 0]^T,
\end{aligned} \tag{B.6}$$

and

$$\boldsymbol{K}=\begin{bmatrix} 1 & -1 & -1 & 0 & 0\\ \mu_1^{\text{ax}} & -\mu_2^{rz}\xi_1 & -\mu_2^{rz}\xi_2 & 0 & 0\\ 0 & \sqrt{\phi_c}^{1-\xi_1} & \sqrt{\phi_c}^{1-\xi_2} & -1 & -1\\ 0 & \mu_2^{rz}\xi_1\sqrt{\phi_c}^{1-\xi_1} & \mu_2^{rz}\xi_2\sqrt{\phi_c}^{1-\xi_2} & -\mu_0^{\text{ax}} & \mu_0^{\text{ax}}\\ 0 & 0 & 0 & 1 & \phi_m \end{bmatrix}. \tag{B.7}$$

The solution of the above system can be written in the general form

$$\boldsymbol{\Xi}=2\beta\boldsymbol{\Xi}^\beta+\sum_{i=0}^{2}s_i\boldsymbol{\Xi}^{s_i}. \tag{B.8}$$

From the relations (B.2) and (B.8) one obtains

$$2\varepsilon_{i_{13}}=A_{i_{xz}}2\bar{\varepsilon}_{13}+\sum_{j=0}^{2}A^p_{j,i_{xz}}\sigma^p_{j_{13}},\quad \sigma_{i_{13}}=D_{i_{xz}}2\bar{\varepsilon}_{13}+\sum_{j=0}^{2}D^p_{j,i_{xz}}\sigma^p_{j_{13}}, \tag{B.9}$$

with

$$A_{1_{xz}}=\Xi^\beta_{1,1},A_{2_{xz}}=\sum_{j=1}^{2}\Phi_j\Xi^\beta_{2,j},A_{0_{xz}}=\Xi^\beta_{0,1},$$

$$D_{1_{xz}}=\mu_1^{\text{ax}}\Xi^\beta_{1,1},D_{2_{xz}}=\mu_2^{rz}\sum_{j=1}^{2}\xi_j\Phi_j\Xi^\beta_{2,j},D_{0_{xz}}=\mu_0^{\text{ax}}\Xi^\beta_{0,1},$$

$$A^p_{i,1_{xz}}=\Xi^{s_i}_{1,1},\quad A^p_{i,2_{xz}}=\sum_{j=1}^{2}\Phi_j\Xi^{s_i}_{2,j},\quad A^p_{i,0_{xz}}=\Xi^{s_i}_{0,1},\quad i=0,1,2,$$

$$\begin{aligned}
D^p_{i,1_{xz}}&=\delta_{i1}+\mu_1^{\text{ax}}\Xi^{s_i}_{1,1},\\
D^p_{i,2_{xz}}&=\delta_{i2}+\mu_2^{rz}\sum_{j=1}^{2}\xi_j\Phi_j\Xi^{s_i}_{2,j},\\
D^p_{i,0_{xz}}&=\delta_{i0}+\mu_0^{\text{ax}}\Xi^{s_i}_{0,1},\quad i=0,1,2.
\end{aligned}$$

B.2. Transverse normal conditions

For the fields presented in Section 3.3, the average strains and stresses at every phase are given by the formulas

$$\begin{aligned}
\boldsymbol{\varepsilon}_1&=\Xi_{1,1}\boldsymbol{I}_{x-y},\\
\boldsymbol{\varepsilon}_2&=\sum_{i=1}^{2}\Phi_i\Xi_{2,i}\boldsymbol{I}_{x-y},\\
\boldsymbol{\varepsilon}_0&=\Xi_{0,1}\boldsymbol{I}_{x-y},\\
\boldsymbol{\sigma}_1&=\left[s_1+2K_1^{\text{tr}}\Xi_{1,1}\right]\\
\boldsymbol{I}_{x-y}&\quad+2l_1\Xi_{1,1}\boldsymbol{I}_z,\\
\boldsymbol{\sigma}_2&=[s_2+\Sigma_2^x]\boldsymbol{I}_{x-y}+\Sigma_2^z\boldsymbol{I}_z,\\
\boldsymbol{\sigma}_0&=\left[s_0+2K_0^{\text{tr}}\Xi_{0,1}\right]\\
\boldsymbol{I}_{x-y}&\quad+2l_0\Xi_{0,1}\boldsymbol{I}_z,
\end{aligned} \tag{B.10}$$

with

$$\boldsymbol{I}_{x-y}=[1\quad 1\quad 0\quad 0\quad 0\quad 0]^T,\quad \boldsymbol{I}_z=[0\quad 0\quad 1\quad 0\quad 0\quad 0]^T, \tag{B.11}$$

$$\Phi_i = \frac{\sqrt{\phi_c}^{1-\xi_i} - \phi_c}{1-\phi_c}, \tag{B.12}$$

and

$$\begin{aligned} \Sigma_2^x &= \sum_{i=1}^{2} \Sigma_{2,i}^x \Xi_{2,i}, \quad \Sigma_{2,i}^x = [L_2^{r\theta} + L_2^{rr}\xi_i]\Phi_i, \\ \Sigma_2^z &= \sum_{i=1}^{2} \Sigma_{2,i}^z \Xi_{2,i}, \quad \Sigma_{2,i}^z = 2\frac{L_2^{\theta z} + L_2^{rz}\xi_i}{1+\xi_i}\Phi_i. \end{aligned} \tag{B.13}$$

Using the interface and boundary conditions one obtains the linear system

$$\boldsymbol{K}\cdot\boldsymbol{\Xi} = \beta\boldsymbol{F}_\beta + \sum_{i=0}^{2} s_i \boldsymbol{F}_i, \tag{B.14}$$

where

$$\begin{aligned} \boldsymbol{\Xi} &= [\,\Xi_{1,1} \quad \Xi_{2,1} \quad \Xi_{2,2} \quad \Xi_{0,1} \quad \Xi_{0,2}\,]^T, \\ \boldsymbol{F}_\beta &= [\,0 \quad 0 \quad 0 \quad 0 \quad 1\,]^T, \\ \boldsymbol{F}_1 &= [\,0 \quad -1 \quad 0 \quad 0 \quad 0\,]^T, \\ \boldsymbol{F}_2 &= [\,0 \quad 1 \quad 0 \quad -1 \quad 0\,]^T, \\ \boldsymbol{F}_0 &= [\,0 \quad 0 \quad 0 \quad 1 \quad 0\,]^T, \end{aligned} \tag{B.15}$$

and

$$\boldsymbol{K} = \begin{bmatrix} 1 & -1 & -1 & 0 & 0 \\ 2K_1^{\mathrm{tr}} & -[L_2^{r\theta} + L_2^{rr}\xi_1] & -[L_2^{r\theta} + L_2^{rr}\xi_2] & 0 & 0 \\ 0 & \sqrt{\phi_c}^{1-\xi_1} & \sqrt{\phi_c}^{1-\xi_2} & -1 & -1 \\ 0 & [L_2^{r\theta} + L_2^{rr}\xi_1]\sqrt{\phi_c}^{1-\xi_1} & [L_2^{r\theta} + L_2^{rr}\xi_2]\sqrt{\phi_c}^{1-\xi_2} & -2K_0^{\mathrm{tr}} & 2\mu_0^{\mathrm{tr}} \\ 0 & 0 & 0 & 1 & \phi_m \end{bmatrix}. \tag{B.16}$$

The solution of the above system can be written in the general form

$$\boldsymbol{\Xi} = \beta\boldsymbol{\Xi}^\beta + \sum_{i=0}^{2} s_i \boldsymbol{\Xi}^{s_i}. \tag{B.17}$$

From the relations (B.10) and (B.17) one obtains

$$\begin{aligned} \varepsilon_{i_{22}} = \varepsilon_{i_{11}} &= \tfrac{1}{2}A_{i_{xx}}[\bar{\varepsilon}_{11} + \bar{\varepsilon}_{22}] + \tfrac{1}{2}\sum_{j=0}^{2} A_{j,i_{xx}}^p [\sigma_{j_{11}}^p + \sigma_{j_{22}}^p], \\ \sigma_{i_{22}} = \sigma_{i_{11}} &= \tfrac{1}{2}D_{i_{xx}}[\bar{\varepsilon}_{11} + \bar{\varepsilon}_{22}] + \tfrac{1}{2}\sum_{j=0}^{2} D_{j,i_{xx}}^p [\sigma_{j_{11}}^p + \sigma_{j_{22}}^p], \\ \sigma_{i_{33}} &= \tfrac{1}{2}D_{i_{x/x}}[\bar{\varepsilon}_{11} + \bar{\varepsilon}_{22}] + \tfrac{1}{2}\sum_{j=0}^{2} D_{j,i_{x/x}}^p [\sigma_{j_{11}}^p + \sigma_{j_{22}}^p], \end{aligned} \tag{B.18}$$

with

$$A_{1_{xx}} = \Xi_{1,1}^\beta, \quad A_{2_{xx}} = \sum_{j=1}^{2}\Phi_j \Xi_{2,j}^\beta, \quad A_{0_{xx}} = \Xi_{0,1}^\beta,$$

$$D_{1_{xx}} = 2K_1^{\mathrm{tr}}\Xi_{1,1}^\beta, \quad D_{2_{xx}} = \sum_{j=1}^{2}\Sigma_{2,j}^x \Xi_{2,j}^\beta, \quad D_{0_{xx}} = 2K_0^{\mathrm{tr}}\Xi_{0,1}^\beta,$$

$$D_{1_{x/x}} = 2l_1\Xi_{1,1}^\beta, \quad D_{2_{x/x}} = \sum_{j=1}^{2}\Sigma_{2,j}^z \Xi_{2,j}^\beta, \quad D_{0_{x/x}} = 2l_0\Xi_{0,1}^\beta,$$

$$A_{i,1_{xx}}^p = \Xi_{1,1}^{s_i}, \quad A_{i,2_{xx}}^p = \sum_{j=1}^{2}\Phi_j \Xi_{2,j}^{s_i}, A_{i,0_{xx}}^p = \Xi_{0,1}^{s_i}, \quad i = 0,1,2,$$

$$D_{i,1_{x/x}}^p = 2l_1\Xi_{1,1}^{s_i}, \quad D_{i,2_{x/x}}^p = \sum_{j=1}^{2}\Sigma_{2,j}^z \Xi_{2,j}^{s_i}, \quad D_{i,0_{x/x}}^p = 2l_0\Xi_{0,1}^{s_i}, \quad i = 0,1,2,$$

$$\begin{aligned} D_{i,1_{xx}}^p &= \delta_{i1} + 2K_1^{\mathrm{tr}}\Xi_{1,1}^{s_i}, \\ D_{i,2_{xx}}^p &= \delta_{i2} + \sum_{j=1}^{2}\Sigma_{2,j}^x \Xi_{2,j}^{s_i}, \\ D_{i,0_{xx}}^p &= \delta_{i0} + 2K_0^{\mathrm{tr}}\Xi_{0,1}^{s_i}, \quad i = 0,1,2. \end{aligned}$$

B.3. Axial conditions

For the fields presented in Section 3.4, the average strains and stresses at every phase are given by the formulas

$$\begin{aligned} \boldsymbol{\varepsilon}_1 &= \Xi_{1,1}\boldsymbol{I}_{x-y} + \beta\boldsymbol{I}_z, \\ \boldsymbol{\varepsilon}_2 &= \left[\beta\gamma_2 + \sum_{i=1}^{2}\Phi_i\Xi_{2,i}\right]\boldsymbol{I}_{x-y} + \beta\boldsymbol{I}_z, \\ \boldsymbol{\varepsilon}_0 &= \Xi_{0,1}\boldsymbol{I}_{x-y} + \beta\boldsymbol{I}_z, \\ \boldsymbol{\sigma}_1 &= \Sigma_1^x\boldsymbol{I}_{x-y} \\ &\quad + [s_1 + \Sigma_1^z]\boldsymbol{I}_z, \\ \boldsymbol{\sigma}_2 &= [\Sigma_2^x + S_2^x\beta]\boldsymbol{I}_{x-y} + [s_2 + \Sigma_2^z + S_2^z\beta]\boldsymbol{I}_z, \\ \boldsymbol{\sigma}_0 &= \Sigma_0^x\boldsymbol{I}_{x-y} + [s_0 + \Sigma_0^z]\boldsymbol{I}_z, \end{aligned} \tag{B.19}$$

with

$$\begin{aligned} \Sigma_1^x &= 2K_1^{\mathrm{tr}}\Xi_{1,1} + l_1\beta, \quad \Sigma_1^z = 2l_1\Xi_{1,1} + n_1\beta, \\ S_2^x &= \frac{L_2^{\theta z}[L_2^{rr}+L_2^{r\theta}] - L_2^{rz}[L_2^{\theta\theta}+L_2^{r\theta}]}{L_2^{rr}-L_2^{\theta\theta}}, \\ S_2^z &= \frac{[L_2^{\theta z}-L_2^{rz}][L_2^{\theta z}+L_2^{rz}]}{L_2^{rr}-L_2^{\theta\theta}} + L_2^{zz}, \\ \Sigma_0^x &= 2K_0^{\mathrm{tr}}\Xi_{0,1} + l_0\beta, \quad \Sigma_0^z = 2l_0\Xi_{0,1} + n_0\beta. \end{aligned} \tag{B.20}$$

In the above expressions, Σ_2^x, Σ_2^z are given by (B.13) and Φ_i is given by (B.12). Using the interface and boundary conditions one obtains the linear system

$$\boldsymbol{K}\cdot\boldsymbol{\Xi} = \beta\boldsymbol{F}_\beta, \tag{B.21}$$

where

$$\begin{aligned} \boldsymbol{\Xi} &= [\,\Xi_{1,1} \quad \Xi_{2,1} \quad \Xi_{2,2} \quad \Xi_{0,1} \quad \Xi_{0,2}\,]^T, \\ \boldsymbol{F}_\beta &= [\,\gamma_2 \quad \lambda_1 \quad -\gamma_2 \quad -\lambda_0 \quad 0\,]^T, \\ \lambda_1 &= \left[L_2^{r\theta} + L_2^{rr}\right]\gamma_2 + L_2^{rz} - l_1, \\ \lambda_0 &= \left[L_2^{r\theta} + L_2^{rr}\right]\gamma_2 + L_2^{rz} - l_0, \end{aligned} \tag{B.22}$$

and $\boldsymbol{K}$ is given by (B.16). The solution of the above system can be written in the general form

$$\boldsymbol{\Xi} = \beta\boldsymbol{\Xi}^\beta. \tag{B.23}$$

From the relations (B.19) and (B.23) one obtains

$$\begin{aligned} &\varepsilon_{i_{22}} = \varepsilon_{i_{11}} = A_{i_{x-z}}\bar{\varepsilon}_{33}, \varepsilon_{i_{33}} = \bar{\varepsilon}_{33}, \\ &\sigma_{i_{22}} = \sigma_{i_{11}} = D_{i_{x-z}}\bar{\varepsilon}_{33}, \sigma_{i_{33}} = D_{i_z}\bar{\varepsilon}_{33} + \sum_{j=0}^{2}\delta_{ji}\sigma_{j_{33}}^p, \end{aligned} \tag{B.24}$$

with

$$A_{1_{x-z}} = \Xi_{1,1}^\beta, \quad A_{2_{x-z}} = \gamma_2 + \sum_{j=1}^{2}\Phi_j\Xi_{2,j}^\beta, \quad A_{0_{x-z}} = \Xi_{0,1}^\beta,$$

$$D_{1_{x-z}} = l_1 + 2K_1^{\mathrm{tr}}\Xi_{1,1}^\beta, \quad D_{2_{x-z}} = S_2^x + \sum_{j=1}^{2}\Sigma_{2,j}^x\Xi_{2,j}^\beta, \quad D_{0_{x-z}} = l_0 + 2K_0^{\mathrm{tr}}\Xi_{0,1}^\beta,$$

$$D_{1_z} = n_1 + 2l_1\Xi_{1,1}^\beta, \quad D_{2_z} = S_2^z + \sum_{j=1}^{2}\Sigma_{2,j}^z\Xi_{2,j}^\beta, \quad D_{0_z} = n_0 + 2l_0\Xi_{0,1}^\beta,$$

for $i = 0,1,2$, and $\Sigma_{2,j}^x, \Sigma_{2,j}^z$ are given by (B.13).

B.4. Transverse shear conditions

For the fields presented in Section 3.5, the average strains and stresses at every phase are given by the formulas

$$\begin{aligned}
\boldsymbol{\varepsilon}_1 &= [[1+Z_1]\Xi_{1,1}+2\Xi_{1,2}]\boldsymbol{I}_{xy},\\
\boldsymbol{\varepsilon}_2 &= \sum_{i=1}^{4}[1+X_i]\Phi_i\Xi_{2,i}\boldsymbol{I}_{xy},\\
\boldsymbol{\varepsilon}_0 &= \left[\tfrac{1+\phi_m}{\phi_m}[1+Z_0]\Xi_{0,1}+2\Xi_{0,2}\right]\boldsymbol{I}_{xy},\\
\boldsymbol{\sigma}_1 &= [s_1+\mu_1^{\mathrm{tr}}[[1+Z_1]\Xi_{1,1}+2\Xi_{1,2}]]\boldsymbol{I}_{xy},\\
\boldsymbol{\sigma}_2 &= \left[s_2+\sum_{i=1}^{4}\tfrac{W_i\Phi_i}{2[1+\xi_i]}\Xi_{2,i}\right]\boldsymbol{I}_{xy},\\
\boldsymbol{\sigma}_0 &= \left[s_0+\mu_0^{\mathrm{tr}}\left[\tfrac{1+\phi_m}{\phi_m}[1+Z_0]\Xi_{0,1}+2\Xi_{0,2}\right]\right]\boldsymbol{I}_{xy},
\end{aligned} \tag{B.25}$$

with

$$\boldsymbol{I}_{xy}=[0\quad 0\quad 0\quad 1\quad 0\quad 0]^T, \tag{B.26}$$

$$\Phi_i=\frac{\sqrt{\phi_c}^{1-\xi_i}-\phi_c}{1-\phi_c}, \tag{B.27}$$

$$W_i=[2-X_i][L_2^{\theta\theta}-L_2^{r\theta}]+2\mu_2^{r\theta}[2X_i+\xi_i-1]+X_i\xi_i[L_2^{rr}-L_2^{r\theta}]. \tag{B.28}$$

Let's consider the equivalent medium under the same boundary conditions, and subjected to the inelastic stresses

$$\bar{\sigma}_{rr}^p=\bar{s}\sin 2\theta,\quad \bar{\sigma}_{\theta\theta}^p=-\bar{s}\sin 2\theta,\quad \bar{\sigma}_{r\theta}^p=\bar{s}\cos 2\theta. \tag{B.29}$$

The displacement field at every position is given by the homogeneous solution

$$\bar{u}_r(r,\theta)=\frac{\beta r}{2\bar{\mu}^{\mathrm{tr}}}\sin 2\theta,\quad \bar{u}_\theta(r,\theta)=\frac{\beta r}{2\bar{\mu}^{\mathrm{tr}}}\cos 2\theta,\quad \bar{u}_z=0.$$

The macroscopic strain and stress are given by the formula

$$\bar{\boldsymbol{\varepsilon}}=\frac{\beta}{\bar{\mu}^{\mathrm{tr}}}\boldsymbol{I}_{xy},\quad \bar{\boldsymbol{\sigma}}=\beta\boldsymbol{I}_{xy}. \tag{B.30}$$

From the Eshelby's energy principle, one finds the relation (Christensen, 1979)

$$\begin{aligned}
&\int_{-L}^{L}\int_0^{2\pi}\Big[\sigma_{rr}^{(3)}\bar{u}_r+\sigma_{r\theta}^{(3)}\bar{u}_\theta+\sigma_{rz}^{(3)}\bar{u}_z\\
&-\bar{\sigma}_{rr}\bar{u}_r^{(3)}-\bar{\sigma}_{r\theta}u_\theta^{(3)}-\bar{\sigma}_{rz}u_z^{(3)}\Big]_{r=r_0}d\theta dz=0.
\end{aligned} \tag{B.31}$$

The latter leads to

$$[2[\bar{K}^{\mathrm{tr}}+\bar{\mu}^{\mathrm{tr}}]\beta+[\bar{K}^{\mathrm{tr}}+2\bar{\mu}^{\mathrm{tr}}]\bar{s}]\bar{\Xi}_4=0, \tag{B.32}$$

which implies that $\bar{\Xi}_4=0$.

Using the interface conditions at $r=r_1, r=r_2$, the traction continuity conditions at $r=r_0$ and the result of the Eshelby's energy principle, one obtains the system

$$\boldsymbol{K}\cdot\boldsymbol{\Xi}=\beta\boldsymbol{F}_\beta+\bar{s}\bar{\boldsymbol{F}}+\bar{\Xi}_3\boldsymbol{F}_3+\sum_{i=0}^{2}s_1\boldsymbol{F}_i, \tag{B.33}$$

where

$$\begin{aligned}
\boldsymbol{\Xi} &= [\Xi_{1,1}\quad \Xi_{1,2}\quad \Xi_{2,1}\quad \Xi_{2,2}\quad \Xi_{2,3}\quad \Xi_{2,4}\quad \Xi_{0,1}\quad \Xi_{0,2}\quad \Xi_{0,3}\quad \Xi_{0,4}]^T,\\
\boldsymbol{F}_\beta &= [0\quad 0\quad 0\quad 0\quad 0\quad 0\quad 0\quad 0\quad 1\quad 1]^T,\\
\bar{\boldsymbol{F}} &= [0\quad 0\quad 0\quad 0\quad 0\quad 0\quad 0\quad 0\quad 1\quad 1]^T,\\
\boldsymbol{F}_3 &= [0\quad 0\quad 0\quad 0\quad 0\quad 0\quad 0\quad 0\quad 3\quad -3]^T,\\
\boldsymbol{F}_1 &= [0\quad 0\quad -1\quad -1\quad 0\quad 0\quad 0\quad 0\quad 0\quad 0]^T,\\
\boldsymbol{F}_2 &= [0\quad 0\quad 1\quad 1\quad 0\quad 0\quad -1\quad -1\quad 0\quad 0]^T,\\
\boldsymbol{F}_0 &= [0\quad 0\quad 0\quad 0\quad 0\quad 0\quad 1\quad 1\quad -1\quad -1]^T,
\end{aligned} \tag{B.34}$$

$$\boldsymbol{K}=\begin{bmatrix}
Z_1 & 1 & -X_1 & -X_2 & -X_3 & -X_4 & 0 & 0 & 0 & 0\\
1 & 1 & -1 & -1 & -1 & -1 & 0 & 0 & 0 & 0\\
0 & 2\mu_1^{\mathrm{tr}} & K_{3,3} & K_{3,4} & K_{3,5} & K_{3,6} & 0 & 0 & 0 & 0\\
2\mu_1^{\mathrm{tr}}[1+Z_1] & 2\mu_1^{\mathrm{tr}} & K_{4,3} & K_{4,4} & K_{4,5} & K_{4,6} & 0 & 0 & 0 & 0\\
0 & 0 & K_{5,3} & K_{5,4} & K_{5,5} & K_{5,6} & -Z_0 & -1 & 1 & -Z_0\\
0 & 0 & K_{6,3} & K_{6,4} & K_{6,5} & K_{6,6} & -1 & -1 & -1 & -1\\
0 & 0 & K_{7,3} & K_{7,4} & K_{7,5} & K_{7,6} & 0 & -2\mu_0^{\mathrm{tr}} & -6\mu_0^{\mathrm{tr}} & 4K_0^{\mathrm{tr}}\\
0 & 0 & K_{8,3} & K_{8,4} & K_{8,5} & K_{8,6} & -2\mu_0^{\mathrm{tr}}[1+Z_0] & -2\mu_0^{\mathrm{tr}} & 6\mu_0^{\mathrm{tr}} & -2K_0^{\mathrm{tr}}\\
0 & 0 & 0 & 0 & 0 & 0 & 0 & 2\mu_0^{\mathrm{tr}} & 6\mu_0^{\mathrm{tr}}\phi_m^2 & -4K_0^{\mathrm{tr}}\phi_m\\
0 & 0 & 0 & 0 & 0 & 0 & 2\mu_0^{\mathrm{tr}}[1+Z_0]\frac{1}{\phi_m} & 2\mu_0^{\mathrm{tr}} & -6\mu_0^{\mathrm{tr}}\phi_m^2 & 2K_0^{\mathrm{tr}}\phi_m
\end{bmatrix}, \tag{B.35}$$

and

$$\begin{aligned}
K_{3,i+2} &= -L_2^{r\theta}[X_i-2]-L_2^{rr}X_i\xi_i,\\
K_{4,i+2} &= -\mu_2^{r\theta}[2X_i+\xi_i-1],\\
K_{5,i+2} &= X_i\sqrt{\phi_c}^{1-\xi_i},\\
K_{6,i+2} &= \sqrt{\phi_c}^{1-\xi_i},\\
K_{7,i+2} &= \left[L_2^{r\theta}[X_i-2]+L_2^{rr}X_i\xi_i\right]\sqrt{\phi_c}^{1-\xi_i},\\
K_{8,i+2} &= \mu_2^{r\theta}[2X_i+\xi_i-1]\sqrt{\phi_c}^{1-\xi_i},
\end{aligned} \tag{B.36}$$

for $i=1,2,3,4$. Solving the above system, the Ξ terms are split in two parts and are given in the compact form

$$\begin{aligned}
\boldsymbol{\Xi}_f &= \beta\boldsymbol{\Xi}_f^\beta+\bar{s}\boldsymbol{\Xi}_f^s+\bar{\Xi}_3\boldsymbol{\Xi}_f^3+\sum_{i=0}^{2}s_i\boldsymbol{\Xi}_f^{s_i},\\
\boldsymbol{\Xi}_0 &= \beta\boldsymbol{\Xi}_0^\beta+\bar{s}\boldsymbol{\Xi}_0^s+\bar{\Xi}_3\boldsymbol{\Xi}_0^3+\sum_{i=0}^{2}s_i\boldsymbol{\Xi}_0^{s_i},
\end{aligned} \tag{B.37}$$

where

$$\begin{aligned}
\boldsymbol{\Xi}_f^w &= [\Xi_{1,1}^w\quad \Xi_{1,2}^w\quad \Xi_{2,1}^w\quad \Xi_{2,2}^w\quad \Xi_{2,3}^w\quad \Xi_{2,4}^w]^T,\\
\boldsymbol{\Xi}_0^w &= [\Xi_{0,1}^w\quad \Xi_{0,2}^w\quad \Xi_{0,3}^w\quad \Xi_{0,4}^w]^T,
\end{aligned} \tag{B.38}$$

and w is empty index or any of the indices β, s_1, s_2, s_0, s and 3. The last two interface conditions (displacement continuity at $r=r_0$) give the system

$$\begin{bmatrix} \frac{Z_0}{\phi_m} & 1 & -\phi_m^2 & Z_0'\phi_m \\ \frac{1}{\phi_m} & 1 & \phi_m^2 & \phi_m \end{bmatrix} \cdot \begin{bmatrix} \Xi_{0,1} \\ \Xi_{0,2} \\ \Xi_{0,3} \\ \Xi_{0,4} \end{bmatrix} = \frac{\beta}{2\bar{\mu}^{\rm tr}} \begin{bmatrix} 1 \\ 1 \end{bmatrix} + \bar{\Xi}_3 \frac{1}{2\bar{\mu}^{\rm tr}} \begin{bmatrix} -1 \\ 1 \end{bmatrix}, \tag{B.39}$$

or, in compact form,

$$\boldsymbol{\Lambda} \cdot \boldsymbol{\Xi}_0 = \frac{\beta}{2\bar{\mu}^{\rm tr}} \boldsymbol{M}_a + \bar{\Xi}_3 \frac{1}{2\bar{\mu}^{\rm tr}} \boldsymbol{M}_b. \tag{B.40}$$

Splitting the $\bar{\Xi}_3$ into an elastic and an inelastic part,

$$\bar{\Xi}_3 = \bar{\Xi}_3^e + \bar{\Xi}_3^p, \tag{B.41}$$

the substitution of (B.37) in (B.40) yields

$$\begin{aligned} &\left[\beta\left[\boldsymbol{\Lambda} \cdot \boldsymbol{\Xi}_0^\beta - \tfrac{1}{2\bar{\mu}^{\rm tr}} \boldsymbol{M}_a\right] + \bar{\Xi}_3^e \left[\boldsymbol{\Lambda} \cdot \boldsymbol{\Xi}_0^3 - \tfrac{1}{2\bar{\mu}^{\rm tr}} \boldsymbol{M}_b\right]\right] \\ &+ \left[\bar{s}\boldsymbol{\Lambda} \cdot \boldsymbol{\Xi}_0^s + \bar{\Xi}_3^p \left[\boldsymbol{\Lambda} \cdot \boldsymbol{\Xi}_0^3 - \tfrac{1}{2\bar{\mu}^{\rm tr}} \boldsymbol{M}_b\right] + \sum_{i=0}^{2} s_i \boldsymbol{\Lambda} \cdot \boldsymbol{\Xi}_0^{s_i}\right] = 0. \end{aligned} \tag{B.42}$$

Since the inelastic fields are treated as uniform inelastic stresses, the problem remains linear and the principle of superposition holds. Consequently, it is demanded that each one of the two terms of the system (B.42) should be equal to zero for arbitrary choice of β, s_1, s_2 and s_0.

B.4.1. Transverse shear modulus

The first term

$$\beta\left[\boldsymbol{\Lambda} \cdot \boldsymbol{\Xi}_0^\beta - \frac{1}{2\bar{\mu}^{\rm tr}} \boldsymbol{M}_a\right] + \bar{\Xi}_3^e \left[\boldsymbol{\Lambda} \cdot \boldsymbol{\Xi}_0^3 - \frac{1}{2\bar{\mu}^{\rm tr}} \boldsymbol{M}_b\right] = \boldsymbol{0}, \tag{B.43}$$

allows to compute $\bar{\Xi}_3^e$ and $\bar{\mu}^{\rm tr}$. It is a nonlinear system which leads to a quadratic expression for the $\bar{\mu}^{\rm tr}$, which has only one positive solution. For this solution,

$$\bar{\Xi}_3^e = \bar{\Xi}^\beta \beta. \tag{B.44}$$

B.4.2. Transverse shear inelastic stress

Using the obtained value of $\bar{\mu}^{\rm tr}$, the second system

$$\left[\boldsymbol{\Lambda} \cdot \boldsymbol{\Xi}_0^3 - \tfrac{1}{2\bar{\mu}^{\rm tr}} \boldsymbol{M}_b \quad \boldsymbol{\Lambda} \cdot \boldsymbol{\Xi}_0^s\right] \cdot \begin{bmatrix} \bar{\Xi}_3^p \\ \bar{s} \end{bmatrix} = -\sum_{i=0}^{2} s_i \boldsymbol{\Lambda} \cdot \boldsymbol{\Xi}_0^{s_i}, \tag{B.45}$$

is linear and allows to compute $\bar{\Xi}_3^p$ and $\bar{s}$ as functions of s_1, s_2 and s_0. The solution is expressed as

$$\bar{s} = \sum_{i=0}^{2} B_{i_{xy}}^p s_i, \quad \bar{\Xi}_3^p = \sum_{i=0}^{2} \bar{\Xi}^{s_i} s_i. \tag{B.46}$$

B.4.3. Transverse shear concentration tensors

Returning back to (B.37) yields,

$$\begin{aligned} \boldsymbol{\Xi}_f &= \beta\left[\boldsymbol{\Xi}_f^\beta + \bar{\Xi}^\beta \boldsymbol{\Xi}_f^3\right] + \sum_{i=0}^{2} s_i \left[\boldsymbol{\Xi}_f^{s_i} + \bar{\Xi}^{s_i} \boldsymbol{\Xi}_f^3 + B_{i_{xy}}^p \boldsymbol{\Xi}_f^s\right], \\ \boldsymbol{\Xi}_0 &= \beta\left[\boldsymbol{\Xi}_0^\beta + \bar{\Xi}^\beta \boldsymbol{\Xi}_0^3\right] + \sum_{i=0}^{2} s_i \left[\boldsymbol{\Xi}_0^{s_i} + \bar{\Xi}^{s_i} \boldsymbol{\Xi}_0^3 + B_{i_{xy}}^p \boldsymbol{\Xi}_0^s\right]. \end{aligned} \tag{B.47}$$

Regrouping the Ξ terms, one obtains the solution in the general form

$$\boldsymbol{\Xi} = \frac{\beta}{\bar{\mu}^{\rm tr}} \boldsymbol{\Omega}^\beta + \sum_{i=0}^{2} s_i \boldsymbol{\Omega}^{s_i}. \tag{B.48}$$

Combining (B.25) and (B.48), one obtains

$$\begin{aligned} 2\varepsilon_{i_{12}} &= A_{i_{xy}} 2\bar{\varepsilon}_{12} + \sum_{j=0}^{2} A_{j,i_{xy}}^p \sigma_{j_{12}}^p, \\ \sigma_{i_{12}} &= D_{i_{xy}} 2\bar{\varepsilon}_{12} + \sum_{j=0}^{2} D_{j,i_{xy}}^p \sigma_{j_{12}}^p, \end{aligned} \tag{B.49}$$

where

$$\begin{aligned} &A_{1_{xy}} = [1 + Z_1]\Omega_{1,1}^\beta + 2\Omega_{1,2}^\beta, \quad D_{1_{xy}} = \mu_1^{\rm tr} A_{1_{xy}} \\ &A_{2_{xy}} = \sum_{j=1}^{4} [1 + X_j]\Phi_j \Omega_{2,j}^\beta, \quad D_{2_{xy}} = \sum_{j=1}^{4} \tfrac{W_j \Phi_j}{2[1+\xi_j]} \Omega_{2,j}^\beta, \\ &A_{0_{xy}} = \tfrac{1+\phi_m}{\phi_m}[1 + Z_0]\Omega_{0,1}^\beta + 2\Omega_{0,2}^\beta, \quad D_{0_{xy}} = \mu_0^{\rm tr} A_{0_{xy}} \\ &A_{i,1_{xy}}^p = [1 + Z_1]\Omega_{1,1}^{s_i} + 2\Omega_{1,2}^{s_i}, \quad D_{i,1_{xy}}^p = \delta_{i1} + \mu_1^{\rm tr} A_{i,1_{xy}}^p, \\ &A_{i,2_{xy}}^p = \sum_{j=1}^{4} [1 + X_j]\Phi_j \Omega_{2,j}^{s_i}, \quad D_{i,2_{xy}}^p = \delta_{i2} + \sum_{j=1}^{4} \tfrac{W_j \Phi_j}{2[1+\xi_j]} \Omega_{2,j}^{s_i}, \\ &A_{i,0_{xy}}^p = \tfrac{1+\phi_m}{\phi_m}[1 + Z_0]\Omega_{0,1}^{s_i} + 2\Omega_{0,2}^{s_i}, D_{i,0_{xy}}^p = \delta_{i0} + \mu_0^{\rm tr} A_{i,0_{xy}}^p, \end{aligned}$$

for $i = 0, 1, 2$.

B.5. Deviatoric conditions

For the fields presented in Section 3.6, there are many similarities with the transverse shear conditions. The tensor $\boldsymbol{I}_{xy}$ is actually substituted by

$$\boldsymbol{I}_{x/y} = [\,1 \quad -1 \quad 0 \quad 0 \quad 0 \quad 0\,]^T. \tag{B.50}$$

The obtained systems of equations are exactly the same with the (B.33) and (B.39). In addition, (B.25) and (B.30) change to

$$\begin{aligned} \boldsymbol{\varepsilon}_1 &= \tfrac{1}{2}[[1 + Z_1]\Xi_{1,1} + 2\Xi_{1,2}]\boldsymbol{I}_{x/y}, \\ \boldsymbol{\varepsilon}_2 &= \tfrac{1}{2}\sum_{i=1}^{4}[1 + X_i]\Phi_i \Xi_{2,i} \boldsymbol{I}_{x/y}, \\ \boldsymbol{\varepsilon}_0 &= \tfrac{1}{2}\left[\tfrac{1+\phi_m}{\phi_m}[1 + Z_0]\Xi_{0,1} + 2\Xi_{0,2}\right]\boldsymbol{I}_{x/y}, \\ \boldsymbol{\sigma}_1 &= \left[s_1 + \mu_1^{\rm tr}[[1 + Z_1]\Xi_{1,1} + 2\Xi_{1,2}]\right]\boldsymbol{I}_{x/y}, \\ \boldsymbol{\sigma}_2 &= \left[s_2 + \sum_{i=1}^{4} \tfrac{W_i \Phi_i}{2[1+\xi_i]} \Xi_{2,i}\right]\boldsymbol{I}_{x/y}, \\ \boldsymbol{\sigma}_0 &= \left[s_0 + \mu_0^{\rm tr}\left[\tfrac{1+\phi_m}{\phi_m}[1 + Z_0]\Xi_{0,1} + 2\Xi_{0,2}\right]\right]\boldsymbol{I}_{x/y}, \end{aligned} \tag{B.51}$$

and

$$\bar{\boldsymbol{\varepsilon}} = \frac{\beta}{2\bar{\mu}^{\rm tr}} \boldsymbol{I}_{x/y}, \tag{B.52}$$

respectively. Consequently,

$$\begin{aligned} \varepsilon_{i_{11}} &= \tfrac{1}{2} A_{i_{xy}}[\bar{\varepsilon}_{11} - \bar{\varepsilon}_{22}] + \tfrac{1}{4}\sum_{j=0}^{2} A_{j,i_{xy}}^p [\sigma_{j_{11}}^p - \sigma_{j_{22}}^p] = -\varepsilon_{i_{22}}, \\ \sigma_{i_{11}} &= D_{i_{xy}}[\bar{\varepsilon}_{11} - \bar{\varepsilon}_{22}] + \tfrac{1}{2}\sum_{j=0}^{2} D_{j,i_{xy}}^p [\sigma_{j_{11}}^p - \sigma_{j_{22}}^p] = -\sigma_{i_{22}}. \end{aligned} \tag{B.53}$$

B.6. Thermal conditions

For the fields presented in Section 3.8, the average stresses at every phase are given by the formulas

$$\begin{aligned} \boldsymbol{\sigma}_1 &= [2K_1^{\rm tr}\Xi_{1,1} + s_1^{\rm tr}]\boldsymbol{I}_{x-y} + [2l_1\Xi_{1,1} + s_1^{\rm ax}]\boldsymbol{I}_z, \\ \boldsymbol{\sigma}_2 &= [\Sigma_2^x + S_x^r s_2^r + S_x^\theta s_2^\theta]\boldsymbol{I}_{x-y} + [\Sigma_2^z + S_z^r s_2^r + S_z^\theta s_2^\theta + s_2^z]\boldsymbol{I}_z, \\ \boldsymbol{\sigma}_0 &= [2K_0^{\rm tr}\Xi_{0,1} + s_0^{\rm tr}]\boldsymbol{I}_{x-y} + [2l_0\Xi_{0,1} + s_0^{\rm ax}]\boldsymbol{I}_z, \end{aligned} \tag{B.54}$$

with

$$\begin{aligned} S_x^r &= \frac{L_2^{\theta\theta}+L_2^{r\theta}}{L_2^{\theta\theta}-L_2^{rr}}, \quad S_x^\theta = 1 - S_x^r, \\ S_z^r &= \frac{L_2^{rz}+L_2^{\theta z}}{L_2^{\theta\theta}-L_2^{rr}}, \quad S_z^\theta = -S_z^r. \end{aligned} \tag{B.55}$$

and Σ_2^x, Σ_2^z are given by (B.13). Using the interface and boundary conditions one obtains the linear system

$$\boldsymbol{K}\cdot\boldsymbol{\Xi} = s_1^{\rm tr}\boldsymbol{F}_1^{\rm tr} + s_2^r\boldsymbol{F}_2^r + s_2^\theta\boldsymbol{F}_2^\theta + s_0^{\rm tr}\boldsymbol{F}_0^{\rm tr}, \tag{B.56}$$

where

$$\begin{aligned} \boldsymbol{\Xi} &= [\,\Xi_{1,1} \quad \Xi_{2,1} \quad \Xi_{2,2} \quad \Xi_{0,1} \quad \Xi_{0,2}\,]^T, \\ \boldsymbol{F}_1^{\rm tr} &= [\,0 \quad -1 \quad 0 \quad 0 \quad 0\,]^T, \\ \boldsymbol{F}_2^r &= [\,X \quad S_x^r \quad -X \quad -S_x^r \quad 0\,]^T, \\ \boldsymbol{F}_2^\theta &= [\,-X \quad S_x^\theta \quad X \quad -S_x^\theta \quad 0\,]^T, \\ \boldsymbol{F}_0^{\rm tr} &= [\,0 \quad 0 \quad 0 \quad 1 \quad 0\,]^T, \end{aligned} \tag{B.57}$$

and $\boldsymbol{K}$ is given by (B.16). The solution of the above system can be written in the general form

$$\boldsymbol{\Xi} = s_1^{\rm tr}\boldsymbol{\Xi}^{s_1} + s_2^r\boldsymbol{\Xi}^{s_2^r} + s_2^\theta\boldsymbol{\Xi}^{s_2^\theta} + s_0^{\rm tr}\boldsymbol{\Xi}^{s_0}. \tag{B.58}$$

Assuming that the equivalent medium is subjected to the uniform thermal stress

$$\bar{\boldsymbol{\sigma}} = \bar{\boldsymbol{\sigma}}^{\rm th} = \bar{s}^{\rm tr}\boldsymbol{I}_{x-y} + \bar{s}^{\rm ax}\boldsymbol{I}_z, \tag{B.59}$$

the relation $(4)_2$ leads to

$$\begin{aligned} \bar{s}^{\rm tr} &= B_{1_x}^{\rm tr}s_1^{\rm tr} + B_{2_x}^r s_2^r + B_{2_x}^\theta s_2^\theta + B_{0_x}^{\rm tr}s_0^{\rm tr}, \\ \bar{s}^{\rm ax} &= B_{1_z}^{\rm ax}s_1^{\rm ax} + B_{1_z}^{\rm tr}s_1^{\rm tr} + B_{2_z}^r s_2^r + B_{2_z}^\theta s_2^\theta \\ &\quad + B_{2_z}^z s_2^z + B_{0_z}^{\rm ax}s_0^{\rm ax} + B_{0_z}^{\rm tr}s_0^{\rm tr}, \end{aligned} \tag{B.60}$$

where

$$\begin{aligned} B_{1_x}^{\rm tr} &= c_1\left[1 + 2K_1^{\rm tr}\Xi_{1,1}^{s_1}\right] + c_2\sum_{i=1}^{2}\Sigma_{2,i}^x\Xi_{2,i}^{s_1} + 2c_0K_0^{\rm tr}\Xi_{0,1}^{s_1}, \\ B_{2_x}^r &= 2c_1K_1^{\rm tr}\Xi_{1,1}^{s_2^r} + c_2\left[S_x^r + \sum_{i=1}^{2}\Sigma_{2,i}^x\Xi_{2,i}^{s_2^r}\right] + 2c_0K_0^{\rm tr}\Xi_{0,1}^{s_2^r}, \\ B_{2_x}^\theta &= 2c_1K_1^{\rm tr}\Xi_{1,1}^{s_2^\theta} + c_2\left[S_x^\theta + \sum_{i=1}^{2}\Sigma_{2,i}^x\Xi_{2,i}^{s_2^\theta}\right] + 2c_0K_0^{\rm tr}\Xi_{0,1}^{s_2^\theta}, \\ B_{0_x}^{\rm tr} &= 2c_1K_1^{\rm tr}\Xi_{1,1}^{s_0} + c_2\sum_{i=1}^{2}\Sigma_{2,i}^x\Xi_{2,i}^{s_0} + c_0\left[1 + 2K_0^{\rm tr}\Xi_{0,1}^{s_0}\right], \\ B_{1_z}^{\rm ax} &= c_1, \quad B_{2_z}^z = c_2, \quad B_{0_z}^{\rm ax} = c_0, \\ B_{1_z}^{\rm tr} &= 2c_1l_1\Xi_{1,1}^{s_1} + c_2\sum_{i=1}^{2}\Sigma_{2,i}^z\Xi_{2,i}^{s_1} + 2c_0l_0\Xi_{0,1}^{s_1}, \\ B_{2_z}^r &= 2c_1l_1\Xi_{1,1}^{s_2^r} + c_2\left[S_z^r + \sum_{i=1}^{2}\Sigma_{2,i}^z\Xi_{2,i}^{s_2^r}\right] + 2c_0l_0\Xi_{0,1}^{s_2^r}, \\ B_{2_z}^\theta &= 2c_1l_1\Xi_{1,1}^{s_2^\theta} + c_2\left[S_z^\theta + \sum_{i=1}^{2}\Sigma_{2,i}^z\Xi_{2,i}^{s_2^\theta}\right] + 2c_0l_0\Xi_{0,1}^{s_2^\theta}, \\ B_{0_z}^{\rm tr} &= 2c_1l_1\Xi_{1,1}^{s_0} + c_2\sum_{i=1}^{2}\Sigma_{2,i}^z\Xi_{2,i}^{s_0} + 2c_0l_0\Xi_{0,1}^{s_0}. \end{aligned}$$

References

Al-Saleh, M.H., Sundararaj, U., 2011. Review of the mechanical properties of carbon nanofiber/polymer composites. Compos. A 42, 2126–2142.

Avery, W.B., Herakovich, C.T., 1986. Effect of fiber anisotropy on thermal stresses in fibrous composites. J. Appl. Mech. 53, 751–756.

Bal, S., Samal, S.S., 2007. Carbon nanotube reinforced polymer composites – a state of art. Bull. Mater. Sci. 30 (4), 379–386.

Barral, M., Chatzigeorgiou, G., Meraghni, F., Léon, R., 2020. Homogenization using modified Mori-Tanaka and TFA framework for elastoplastic-viscoelastic-viscoplastic composites: theory and numerical validation. Int. J. Plast. 127, 102632.

Batra, R.C., Sears, A., 2007. Uniform radial expansion/contraction of carbon nanotubes and their transverse elastic moduli. Model. Simul. Mater. Sci. Eng. 15, 835–844.

Brassart, L., Stainier, L., Doghri, I., Delannay, L., 2012. Homogenization of elasto-(visco) plastic composites based on an incremental variational principle. Int. J. Plast. 36, 86–112.

Chaboche, J., Kanoute, P., Ross, A., 2005. On the capabilities of mean field approaches for the description of plasticity in metal matrix composites. Int. J. Plast. 21, 1409–1434.

Chatzigeorgiou, G., Charalambakis, N., Chemisky, Y., Meraghni, F., 2018. Thermomechanical Behavior of Dissipative Composite Materials. ISTE Press - Elsevier, London.

Chatzigeorgiou, G., Efendiev, Y., Charalambakis, N., Lagoudas, D.C., 2012. Effective thermoelastic properties of composites with periodicity in cylindrical coordinates. Int. J. Solids Struct. 49 (18), 2590–2603.

Chatzigeorgiou, G., Efendiev, Y., Lagoudas, D.C., 2011. Homogenization of aligned "fuzzy fiber" composites. Int. J. Solids Struct. 48 (19), 2668–2680.

Chatzigeorgiou, G., Meraghni, F., 2019. Elastic and inelastic local strain fields in composites with coated fibers or particles: theory and validation. Math. Mech. Solids 24 (9), 2858–2894.

Chatzigeorgiou, G., Seidel, G.D., Lagoudas, D.C., 2012. Effective mechanical properties of aligned "fuzzy fiber" composites. Compos. B Eng. special issue "Homogenization and Micromechanics of Smart and Multifunctional Materials" 43, 2577–2593..

Chen, T., Dvorak, G.J., Benveniste, Y., 1990. Stress fields in composites reinforced by coated cylindrically orthotropic fibers. Mech. Mater. 9, 17–32.

Christensen, R.M., 1979. Mechanics of Composite Materials. Dover, New York.

Christensen, R.M., Lo, K.H., 1979. Solutions for effective shear properties in three phase sphere and cylinder models. J. Mech. Phys. Solids 27, 315–330.

Dhala, S., Ray, M.C., 2015. Micromechanics of piezoelectric fuzzy fiber-reinforced composite. Mech. Mater. 81, 1–17.

Dvorak, G., 1992. Transformation field analysis of inelastic composite materials. Proc. Roy. Soc. Lond. A 437, 311–327..

Dvorak, G., Benveniste, Y., 1992. On transformation strains and uniform fields in multiphase elastic media. Proc. Roy. Soc. Lond. A 437, 291–310..

Feng, X.Q., Shi, D.L., Huang, Y.G., Hwang, K.C., 2007. Micromechanics and multiscale mechanics of carbon nanotubes-reinforced composites. In: Sih, G.C. (Ed.), Multiscaling in Molecular and Continuum Mechanics: Interaction of Time and Size from Macro to Nano: Application to Biology, Physics, Material Science, Mechanics, Structural and Processing Engineering. Springer, Netherlands, Dordrecht, pp. 103–139.

Guinovart-Sanjuán, D., Rodríguez-Ramos, R., Guinovart-Díaz, R., Bravo-Castillero, J., Sabina, F.J., Merodio, J., Lebon, F., Dumont, S., Conci, A., 2016. Effective properties of regular elastic laminated shell composite. Compos. B 87, 12–20.

Hart, H.C., Koizumi, R., Hamel, J., Owuor, P.S., Ito, Y., Ozden, S., Bhowmick, S., Amanulla, S.A.S., Tsafack, T., Keyshar, K., Mital, R., Hurst, J., Vajtai, R., Tiwary, C. S., Ajayan, P.M., 2017. Velcro-inspired SiC fuzzy fibers for aerospace applications. ACS Appl. Mater. Interfaces 9 (15), 13742–13750.

Hashin, Z., 1990. Thermoelastic properties of fiber composites with imperfect interface. Mech. Mater. 8, 333–348.

Hashin, Z., Rosen, B.W., 1964. The elastic moduli of fiber-reinforced materials. J. Appl. Mech. 31, 223–232.

Honjo, K., 2007. Thermal stresses and effective properties calculated for fiber composites using actual cylindrically-anisotropic properties of interfacial carbon coating. Carbon 45, 865–872.

Hyer, M.W., Waas, A.M., 2000. Micromechanics of linear elastic continuous fiber composites. In: Kelly, A., Zweben, C. (Eds.), Comprehensive Composite Materials, vol. 1. Pergamon, Oxford, pp. 345–375.

Kundalwal, S.I., Meguid, S.A., 2015. Micromechanics modelling of the effective thermoelastic response of nano-tailored composites. Eur. J. Mech. A/Solids 53, 241–253.

Kundalwal, S.I., Ray, M.C., 2011. Micromechanical analysis of fuzzy fiber reinforced composites. Int. J. Mech. Mater. Des. 7, 149–166.

Kundalwal, S.I., Ray, M.C., 2012. Effective properties of a novel continuous fuzzy-fiber reinforced composite using the method of cells and the finite element method. Eur. J. Mech. A/Solids 36, 191–203.

Kundalwal, S.I., Ray, M.C., 2014. Effect of carbon nanotube waviness on the effective thermoelastic properties of a novel continuous fuzzy fiber reinforced composite. Compos. B Eng. 57, 199–209.

Lagoudas, D.C., Gavazzi, A.C., Nigam, H., 1991. Elastoplastic behavior of metal matrix composites based on incremental plasticity and the Mori-Tanaka averaging scheme. Comput. Mech. 8, 193–203.

Lahellec, N., Suquet, P., 2007. On the effective behavior of nonlinear inelastic composites: I. Incremental variational principles. J. Mech. Phys. Solids 55 (9), 1932–1963.

Ma, A.W.K., Yearsley, K.M., Chinesta, F., Mackley, M.R., 2008. A review of the microstructure and rheology of carbon nanotube suspensions. Proc. Inst. Mech. Eng. N J. Nanoeng. Nanosyst. 222 (3), 71–94..

Michel, J.C., Suquet, P., 2003. Nonuniform transformation field analysis. Int. J. Solids Struct. 40, 6937–6955.

Praud, F., 2018. Multi-scale modelling of thermoplastic-based woven composites, cyclic and time-dependent behaviour. Ph.D. thesis, Arts et Métiers ParisTech, Metz.

Ren, X., Burton, J., Seidel, G.D., Lafdi, K., 2015. Computational multiscale modeling and characterization of piezoresistivity in fuzzy fiber reinforced polymer composites. Int. J. Solids Struct. 54, 121–134.

Sager, R.J., Klein, P.J., Lagoudas, D.C., Zhang, Q., Liu, J., Dai, L., Baur, J.W., 2009. Effect of carbon nanotubes on the interfacial shear strength of T650 carbon fiber in an epoxy matrix. Compos. Sci. Technol. 69, 898–904.

Sebastian, J., Schehl, N., Bouchard, M., Boehle, M., Li, L., Lagounov, A., Lafdi, K., 2014. Health monitoring of structural composites with embedded carbon nanotube coated glass fiber sensors. Carbon 66, 191–200.

Seidel, G.D., Chatzigeorgiou, G., Ren, X., Lagoudas, D.C., 2014. Multiscale modeling of multifunctional fuzzy fibers based on multi-walled carbon nanotubes. In: Tserpes, K.I., Silvestre, N.P. (Eds.), Modeling of Carbon Nanotubes, Graphene and their Composites, Springer Series in Materials Science, vol. 188. Springer International Publishing, Cham, pp. 135–176.

Seidel, G.D., Lagoudas, D.C., 2006. Micromechanical analysis of the effective elastic properties of carbon nanotube reinforced composites. Mech. Mater. 38, 884–907.

Shaina, P.R., George, L., Yadav, V., Jaiswal, M., 2016. Estimating the thermal expansion coefficient of graphene: the role of graphene-substrate interactions. J. Phys. Condens. Matter 28, 085301.

Shen, L., Li, J., 2004. Transversely isotropic elastic properties of single-walled carbon nanotubes. Phys. Rev. B 69, 345–414.

Tikarrouchine, E., Chatzigeorgiou, G., Chemisky, Y., Meraghni, F., 2019. Fully coupled thermo-viscoplastic analysis of composite structures by means of multi-scale three-dimensional finite element computations. Int. J. Solids Struct. 164, 120–140.

Tikarrouchine, E., Praud, F., Chatzigeorgiou, G., Piotrowski, B., Chemisky, Y., Meraghni, F., 2018. Three-dimensional FE^2 method for the simulation of non-linear, rate-dependent response of composite structures. Compos. Struct. 193, 165–179.

Tsalis, D., Charalambakis, N., Bonnay, K., Chatzigeorgiou, G., 2017. Effective properties of multiphase composites made of elastic materials with hierarchical structure. Math. Mech. Solids 22 (4), 751–770.

Tsalis, D., Chatzigeorgiou, G., Charalambakis, N., 2012. Homogenization of structures with generalized periodicity. Compos. B Eng., special issue "Homogenization and Micromechanics of Smart and Multifunctional Materials" 43, 2495–2512..

Tsukrov, I., Drach, B., 2010. Elastic deformation of composite cylinders with cylindrically orthotropic layers. Int. J. Solids Struct. 47, 25–33.

Tsukrov, I., Drach, B., Gross, T.S., 2012. Effective stiffness and thermal expansion coefficients of unidirectional composites with fibers surrounded by cylindrical orthotropic matrix layers. Int. J. Eng. Sci. 58, 129–143.

Wu, L., Adam, L., Doghri, I., Noels, L., 2017. An incremental-secant mean-field homogenization method with second statistical moments for elasto-visco-plastic composite materials. Mech. Mater. 114, 180–200.

Xiao, J.R., Gama, B.A., Gillespie, J.W., 2005. An analytical molecular structural mechanics model for the mechanical properties of carbon nanotubes. Int. J. Solids Struct. 42, 3075–3092.

Yanase, K., Moriyama, S., Ju, J.W., 2013. Effects of CNT waviness on the effective elastic responses of CNT-reinforced polymer composites. Acta Mech. 224, 1351–1364.

Zhou, H.W., Mishnaevsky Jr, L., Yi, H.Y., Liu, Y.Q., Hu, X., Warrier, A., Dai, G.M., 2016. Carbon fiber/carbon nanotube reinforced hierarchical composites: effect of CNT distribution on shearing strength. Compos. B 28, 085301.

Zhu, F., Park, C., Yun, G.J., 2020. An extended Mori-Tanaka micromechanics model for wavy CNT nanocomposites with interface damage. Mech. Adv. Mater. Struct. in press.